Periodicity detection methodology in spatially-developing turbulent boundary layers

Matthew Holland[1]*,Christian J. Lagares-Nieves[1,2]† and Guillermo Araya[1]‡
[1]*Computational Turbulence and Visualization Lab., Dept. of Mechanical Eng., University of Texas at San Antonio, TX 78249, USA.*
[1]*Dept. of Mechanical Eng., University of Puerto Rico at Mayaguez, PR 00681, USA.*

Direct Numerical Simulation (DNS) databases of spatially-developing turbulent boundary layers (SDTBL) are scrutinized for detection of spatial/temporal periodic turbulent events. The databases involve incompressible and supersonic (Mach 2.86) flow regimes over isothermal and adiabatic wall thermal conditions at similar low Reynolds numbers ($\delta^+ \approx 250$). Turbulent inflow conditions are modeled via a modified rescaling-recycling approach (J. Fluid Mech. 2011, vol. 670, pp. 581-605). The proposed methodology has been extended to high-speed flows with the consideration of a dynamic procedure to compute "on the fly the ratio" of the inlet friction velocity to the downstream recycle friction velocity with the purpose to bypass the use of any empirical correlation. The principal drawback of any recycling technique is the injection of artificial periodicity on the downstream flow development. In this study, we are assessing the impact of such periodicity on low/high order flow statistics and on the dynamics of coherent structures of Zero Pressure Gradient (ZPG) flows. Major lessons learned are as follows: (i) results based on spatial two-point correlations have shown the existence of strong spatial periodicity between the inlet and recycle planes, (ii) the spatial period is proportional to the inlet-recycle distance and periodic perturbations are convected downstream, (iii) the streamwise component of velocity fluctuations mostly exhibits periodicity, (iv) statistics shows a natural streamwise development of the turbulent boundary layer, (v) periodicity tends to vanish more quickly in time ($\sim$ 300 wall unit time).

I. Nomenclature

CFD	=	Computational Fluid Dynamics
DNS	=	Direct Numerical Simulation
FFT	=	Fast Fourier Transform
FSLE	=	Finite-Size Lyapunov Exponent
FTLE	=	Finite-Time Lyapunov Exponent
IIR	=	Infinite Impulse Response
LCS	=	Lagrangian Coherent Structures
RMS	=	Root Mean Square
SDTBL	=	Spatially Developing Turbulent Boundary Layer
TPC	=	Two-Point Correlation
C_{ij}	=	Right Cauchy-Green strain tensor
E	=	Energy spectra or energy spectral density
F	=	Forcing function
$\mathcal{F}$	=	Fourier Transform operator
$FTLE_N(\mathbf{x}, t)$	=	Finite-Time Lyapunov Exponent at point $\mathbf{x}$ and time t
$\mathbf{k}$	=	Wave vector

*Graduate Research Assistant, Department of Mechanical Engineering, University of Texas at San Antonio, San Antonio, TX, 78249. AIAA Student Member, matthew.holland@my.utsa.edu

†PhD Research Assistant & Doctoral Candidate, Department of Mechanical Engineering, 259 Alfonso Valdez Blvd., Mayaguez, PR, 00680, and Student Member, christian.lagares@upr.edu

‡Associate Professor, Department of Mechanical Engineering, University of Texas at San Antonio, San Antonio, TX, 78249. AIAA Associate Fellow, araya@mailaps.org, https://ceid.utsa.edu/garaya/

$\mathbf{k}^+$	=	Wave vector scaled by the Law of the Wall for Fourier space
λ_{max}	=	Maximum eigenvalue of the right Cauchy-Green strain tensor at $\mathbf{x}$
$\overline{Q_i}$	=	Ensemble averaged flow parameter in a given i direction
q	=	Any flow parameter
q_i	=	Flow parameter in a given i direction
q_i'	=	Fluctuation of flow parameter according to Reynolds decomposition
$\hat{q}$	=	Fluctuation of flow parameter in the Fourier space
R_{ij}	=	Two-Point Correlation between points i and j
$\mathbf{r}$	=	Vector of point that deviates from $\mathbf{x}$
Re	=	Reynolds number
t	=	Time
t^+	=	Wall Time, or time scaled by Law of the Wall
U_i	=	Mean velocity at a given point i
u_i	=	Velocity of flow at a given point i
u_i'	=	Fluctuating component of velocity at a given point i
$\overline{u_i'}$	=	Mean fluctuating velocity
u_τ	=	Friction velocity, as defined by Law of the Wall
$\mathcal{U}_i'$	=	Fluctuating velocity in Fourier space
$\mathcal{U}'^*$	=	Complex conjugate of Fluctuating velocity in Fourier space
y^+	=	Boundary layer height in log law of the wall units
y/δ	=	Boundary layer height normalized to boundary layer thickness
Γ	=	Diffusion of a function
δ	=	Boundary layer thickness
ϵ	=	Error function
ν_w	=	Kinematic velocity of fluid at wall
ρ	=	Can mean either autocorrelation, typically in time, or density, depending on the context
τ	=	Can either denote shear or mean time delay for Fourier series, depending on the context
ϕ	=	Function that convects and diffuses in space
Sub/super scripts	=	
$^+$	=	Wall or inner units
$_{ref}$	=	Parameter at reference location
$_{inl}$	=	Parameter at inlet plane
$_{rec}$	=	Parameter at recycle plane
$_{test}$	=	Parameter at test plane

II. Introduction

Boundary layers are a vital area of fluid mechanics with a wide range of applications. Within these boundary layers, convection, diffusion and friction phenomena happen (i.e., transport phenomena). This is of interest for understanding the behavior of applications ranging from blowing/suction perturbations [1], strong streamwise pressure gradients [2], and high-speed turbulent boundary layers [3, 4]. Shear layers that evolve in space due to turbulent entrainment (particularly, vertical mixing) are the rule not the exception in wall-bounded flows. These boundary layers are not homogeneous in the direction of flow (streamwise direction), and are normally called Spatially-Developing Turbulent Boundary Layers (SDTBL's) [5]. Within these boundary layers are coherent structures that are regions of flow where the fluctuations are highly correlated throughout the time of unsteady flow [5]. It has been reported that within these structures, 60-80% of the Reynolds stress, or average fluctuating force per unit area, occurs within these coherent structures [6], thus making them of great interest to study.

Direct Numerical Simulation (DNS) is an extensive numerical tool to resolve the full spectrum behavior in fluid dynamics, particularly SDTBL's due to their highly fundamental nature and high resolution required to generate adequate data [7]. However, DNS requires large computational resources and storage capabilities. The significant assets required by DNS in transient predictions of SDTBL demands: (i) high-scalable parallel flow solvers, (ii) efficient and robust turbulent inlet conditions, and (iii) small physical time steps, which have certainly restrained the evolution of high spatial/temporal resolution numerical simulations. There are studies that have done DNS to study SDTBL's, and those

have acknowledged the challenges and large resources required to do so [8, 9]. Additionally, if the flow is coming into the computational domain as turbulent, a proper condition for the turbulence is required to calculate the downstream behavior [10]. One method to tackle the challenges of DNS is to break the computational domains up into smaller portions. The flow comes from an auxiliary domain and is initially the flow conditions of that domain, but then solves into the flow behavior of the computational domain [10]. This method can take several forms. One method is to allow the inflow to initially be a flow condition taken from the conditions of an auxiliary domain where the flow in that domain is the outcome of a laminar flow (Blasius solution) triggered to turbulence by resolving the transition stage. This method comes with the advantage of that there are few downstream artifacts of this initialization of the flow [10] but it requires lengthy computational domains. One of the simplest ways of breaking the circular nature of the solving for turbulent inflow conditions is the make the auxiliary domain a flow that is spatially homogeneous in the streamwise direction, which results in initializing the solution from a non-spatially developing flow. This is a highly idealized flow to take the inflow conditions from but allows for a variety of conditions to be used for the inflow. The velocity profiles in terms of both space and time from a station in the auxiliary domain is then taken to be the inlet station for the spatial domain [10].

Rather than having an auxiliary domain, the downstream conditions from one domain are taken to be the inflow conditions for another domain. The handling of inflow turbulence generation was first formulated by Spalart in his 1988 paper describing a multi-scale approach [11]. This was modified by Wu in the 1995 paper, which modified the method by adding a response function to the variance or root mean square (RMS) of velocity. This method assumes that in a zero pressure gradient smooth flat plate boundary layer y^+ scales with the inner region and y/δ scales with the outer region of the boundary layer [12]. At roughly the same time, Lund in his 1998 paper blends the inner and outer regions using a weighting function and scales the time-dependent velocity fields by the friction velocities [13]. Weak recycling reportedly has spurious periodicity, as reported by Simens et al (2009) [14] and Lee and Sung (2011) [15]. Simens was able to find that longer domains used for recycling significantly dampen periodicity, and vice versa [14]. This is the method being studied in-depth in this paper. Rather than going into depth about other inflow methods, namely synthetic methods, a helpful summary is that the inflow conditions can be simplified as a random field described as a randomly generated series of periodic fluctuations [16, 17] or eddies at the inflow of a domain [18]. The validity of these approaches gives insight about the possible nature of turbulence and coherent structures that form. As the flow is more accurately described by a periodic inflow, then the turbulence likely has a strong periodic behavior. As the flow is more accurately described by a synthetic eddy inflow, the turbulence likely has a strong fractal behavior. There are other synthetic methods to define inflow from other sources [10], namely digital twinning [19] and machine learning methods [20]. These methods do not describe the nature of the turbulence and are thus not worth discussing further in this paper.

The major aim of the present study is to identify and assess spatial/temporal periodic turbulent events. Particularly, we are evaluating the repercussion of artificially injected frequencies via flow fluctuations in SDTBL by means of a rescaling-recycling technique for inflow generation.

z

III. DNS Description and Turbulence Statistics

Modeling the physics behind unsteady three-dimensional SDTBL by means of DNS is formidable, due to the following reasons [3]: I) high spatial/temporal resolution required in order to resolve the smallest turbulence length/time scales (Kolmogorov scales for the velocity field and Batchelor scales for the thermal field), II) the computational domain must be large enough to properly capture the effects of large scale motions (Hutchins & Marusic [21]), principally situated in the outer part of the boundary layer, III) realistic time-dependent inflow turbulent conditions (instantaneous velocity, temperature and pressure) must be prescribed. As articulated earlier, one of the crucial aspects on the simulations of unsteady SDTBL is the prescription of accurate turbulent inflow information with the purpose of circumvent the computational-consuming transition stage resolution. In the present manuscript, we use the inflow generation method as in [7], which is a modified version of the original rescaling-recycling method by Lund *et al.* [13]. The core concept of any recycling method is to extract "on the fly" the flow solution (mean and fluctuating components of flow parameters, which depends if the flow is incompressible or compressible, or if one wants to resolve a passive scalar field in incompressible flows) from a downstream plane, called "recycle". Subsequently, scaling law functions are applied to reduce the streamwise inhomogeneity in SDTBL, and finally the transformed flow profiles are re-injected at the inlet plane. Figure 1 shows an schematic of the computational box, iso-surfaces and contours of the instantaneous streamwise velocity. Also, in Fig. 1 the locations of inlet, test and recycle planes are observed. The streamwise distances between

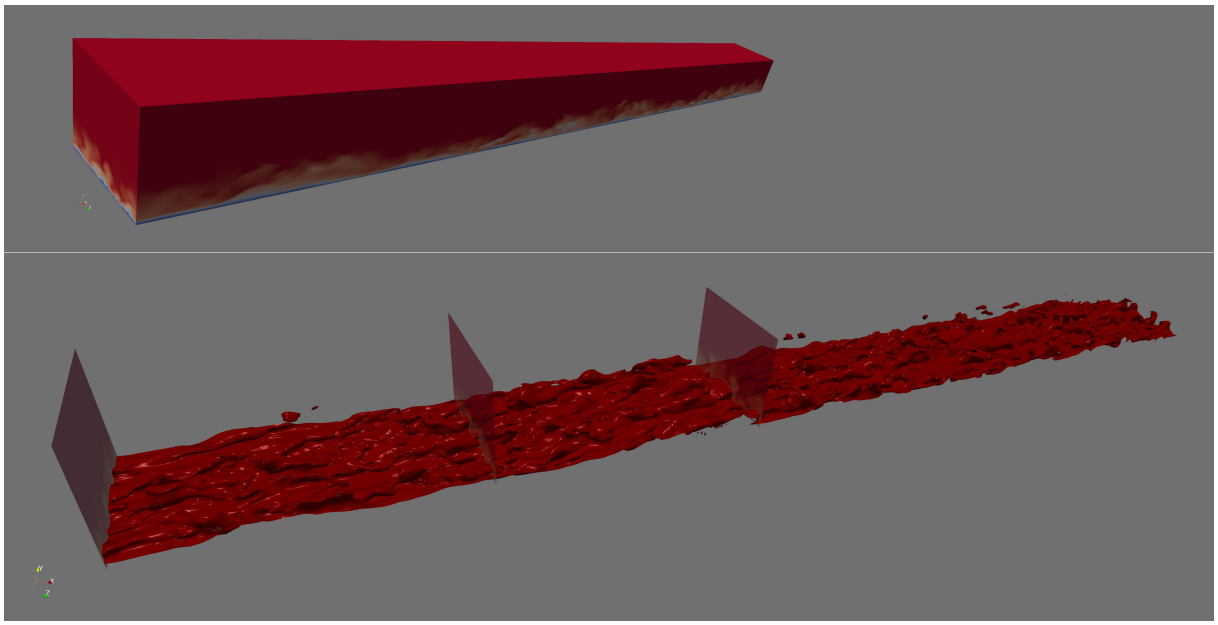

Fig. 1 Schematic of the computational box (about 45δ_{inl} in length) and contours of the instantaneous streamwise velocity (top). Iso-surfaces of instantaneous streamwise velocity (at 75% of U_∞) with cross-sectional YZ planes (Inlet, Test and Recycle planes), flow from left to right.

the inlet and recycle planes are around $17.5 - 18\delta_{inl}$ in all cases analyzed in this study. The Reynolds decomposition is implemented for instantaneous parameters, i.e. a time-averaged plus a fluctuating component:

$$q_i(\mathbf{x}, t) = \overline{Q}_i(x, y) + q_i'(\mathbf{x}, t) \tag{1}$$

where q_i represents instantaneous flow parameter (velocity, temperature or pressure), $\overline{Q}_i$ indicates time-spanwise averaged flow quantity, and q_i' expresses a fluctuating flow quantity. In brief, the turbulent boundary layer is divided into inner and outer zones, where different scaling laws are applied. Extracted flow solution from the recycle plane is projected onto the inlet plane along constant values of y^+ (inner region) and y/δ (outer region). The same blending function to merge inner-outer transformed solutions as employed by [13] was utilized here to obtain the corresponding instantaneous composite flow profiles at the inlet plane. Readers are referred to [7] for additional details.

As described in [3], one of the tasks in the re-scaling process involves computing the ratio of the inlet friction velocity to the recycle friction velocity (i.e., $\lambda = u_{\tau,inl}/u_{\tau,rec}$). The friction velocity is defined as $u_\tau = \sqrt{\tau_w/\rho}$, where τ_w is the wall shear stress and ρ is the fluid density. The inlet boundary layer thickness is prescribed based on the desired inlet Reynolds number to be simulated. Therefore, prescribing also the inlet friction velocity would be redundant in that case. To overcome this issue, Lund *et al.* [13] employed the well-known 1/8-power law that relates the friction velocity to the momentum thickness in zero-pressure gradient flows; thus, $u_{\tau,inl}/u_{\tau,rec} = (\delta_{2,inl}/\delta_{2,rec})^{-1/8}$. The empirical power (-1/8) is strongly affected by the Reynolds number dependency; therefore, we explicitly compute this power, $\gamma_{\delta 2}$, by relating the mean flow solution from a new plane (so-called the "Test" plane, as seen in Figure 1) to the solution from the recycle plane as follows:

$$\gamma_{\delta 2} = \frac{ln(u_{\tau,test}/u_{\tau,rec})}{ln(\delta_{2,test}/\delta_{2,rec})}. \tag{2}$$

Table 1 summarizes the characteristics of the proposed two (2) cases for periodicity evaluation: the incompressible case ($M_\infty = 0$) and supersonic compressible case ($M_\infty = 2.86$) at low Reynolds numbers, $Re_{\delta 2}$. Furthermore, the Reynolds number range, computational domain dimensions in terms of the inlet boundary layer thickness δ_{inl} (where L_x, L_y and L_z represent the streamwise, wall-normal and spanwise domain length, respectively) and mesh resolution in wall units (Δx^+, Δy^+_{min}, Δy^+_{max}, Δz^+) are also given. The number of mesh points in the streamwise, wall-normal, and spanwise direction is $440 \times 60 \times 80$, respectively.

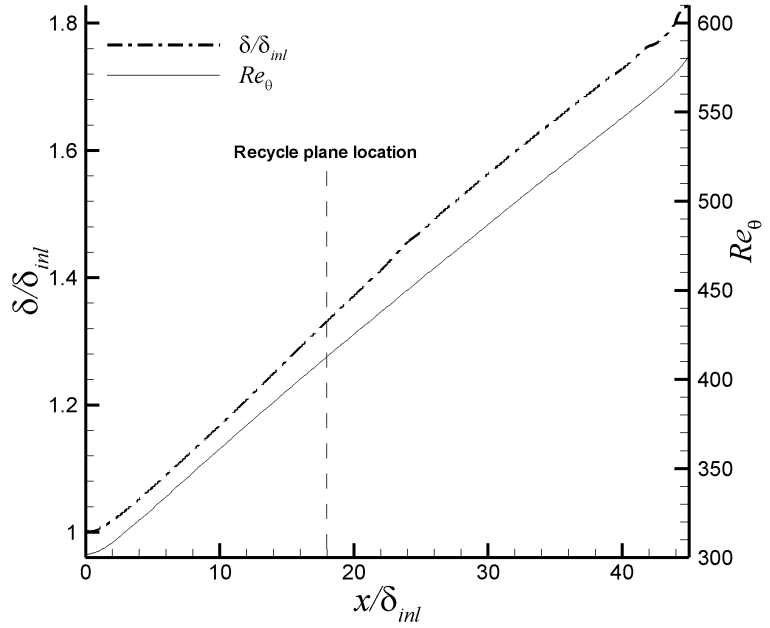

Fig. 2 Streamwise variation of the boundary layer thickness and momentum thickness Reynolds number for the incompressible flow case.

Figure 2 exhibits the streamwise development of the boundary layer thickness (i.e., δ at 99% of U_∞) and the momentum thickness Reynolds number (Re_θ) for the incompressible case. It can be seen an almost linear growing rate for both parameters with a very short inlet developing section (about $2\delta_{inl}$ in length). The location of recycle plane for this case ($\sim$ at $18\delta_{inl}$ from the inlet) is also plotted. Clearly, a natural streamwise evolution of δ and Re_θ is observed upstream and downstream of the recycle plane location. Similarly, the skin friction coefficient, C_f, is depicted by fig. 3 for incompressible flows. After an initial short developing section, C_f profile agrees quite well with the power-law empirical correlation and experiments for incompressible ZPG flows at low Reynolds number by Smits *et al.* [22]. Values of the skin friction coefficient by the domain end show an abnormal increase ("uptick") caused by the outlet boundary condition (pressure prescription). However, penalization on the useful region was completely negligible.
Figure 4 (a) shows time-averaged streamwise velocity profiles in wall units. For supersonic cases, the Van Driest transform was implemented to absorb wall-normal density variation. This allows a fair comparison with incompressible data. Generally speaking, a very good agreement can be observed of present DNS (both, the incompressible and supersonic case) with external DNS from Skote (2011), Pirozzoli and Bernardini (2011), Duan et al. (2011) and Guarini et al. (2000). Similarly, Figure 4 (b) depicts turbulence intensities of present DNS together with external direct simulations from Schlatter and Orlu (2010) and Pirozzoli and Bernardini (2011). Whereas, a fairly good agreement is seen in the inner region of the boundary layer, the Reynolds number dependency is observed in the outer part ($y^+ > 20$) due to the significant difference in Reynolds numbers.

Table 1 DNS Cases.

Case	M_∞	$Re_{\delta 2}$	$L_x \times L_y \times L_z$	Δx^+,Δy^+_{min}/Δy^+_{max}, Δz^+
Incomp.	0	306-578	$45\delta_{inl} \times 3.5\delta_{inl} \times 4.3\delta_{inl}$	14.7, 0.2/13, 8
Supersonic	2.86	468-832	$43.4\delta_{inl} \times 3.5\delta_{inl} \times 4.3\delta_{inl}$	15, 0.2/14, 9

Figure 5 depicts the streamwise development of local maxima of streamwise velocity fluctuations (u') and Reynolds shear stresses ($u'v'$) for the incompressible and supersonic flow cases. The proposed DMA method (turbulent inflow generator) is able to prescribe inlet flow fluctuations with the appropriate energy spectra [5] and wall-normal distribution. Local maxima rapidly tend toward an almost constant value with a non-physical streamwise development region in the order of 3-4δ_{inl}'s at most. For the incompressible case, u' maxima are approximately 14% of the freestream velocity,

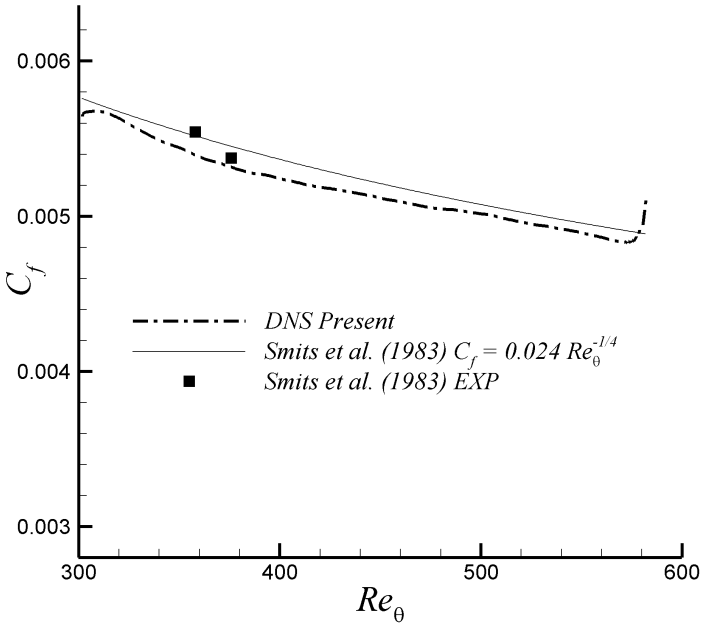

Fig. 3 Streamwise variation of the skin friction coefficient for the incompressible flow case.

U_∞, which is typycal for canonical flat-plate turbulent boundary layers at such low Reynolds numbers. Interestingly, the ratio u'/U_∞ is roughly 15.5 to 16% in the supersonic case, which can be associated with some compressibility effect. On the contrary, peaks of Reynolds shear stresses, $u'v'$, seem quite consistent in both flow regimes ($\approx 0.2\%$ of U_∞^2. In figures 6 and 7 normalized spanwise energy spectra of streamwise velocity fluctuations (E_{uu}) at $y^+ = 100$ and several streamwise locations (including the inlet and recycle plane) are plotted. It can be inferred that inlet power spectra quickly resemble a fully developed downstream spectra with a minimal developing section.

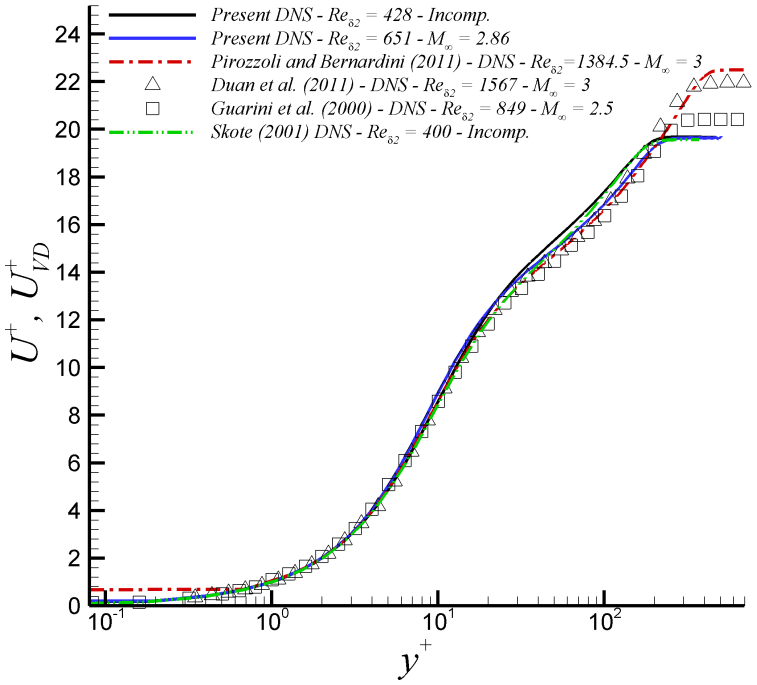

(a)

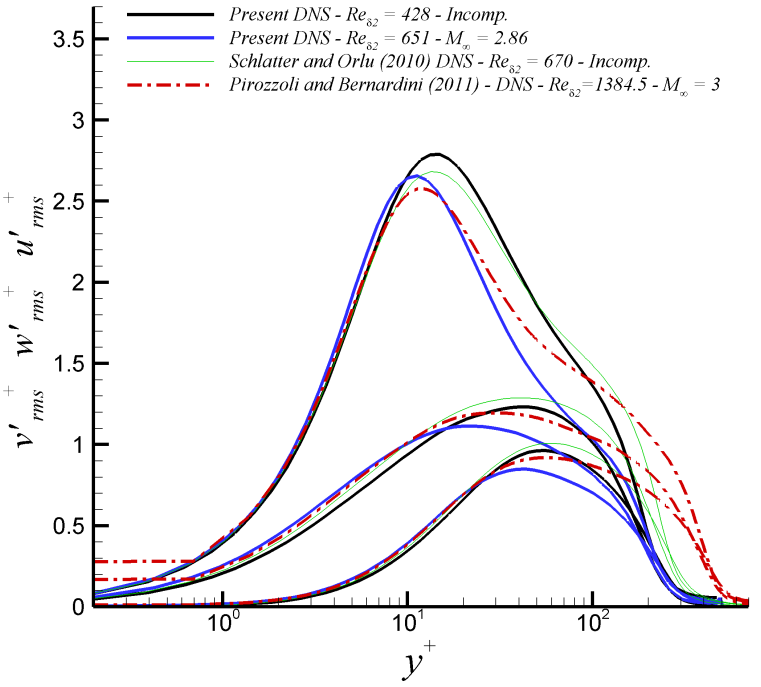

(b)

Fig. 4 (a) Mean streamwise velocity and (b) turbulence intensities.

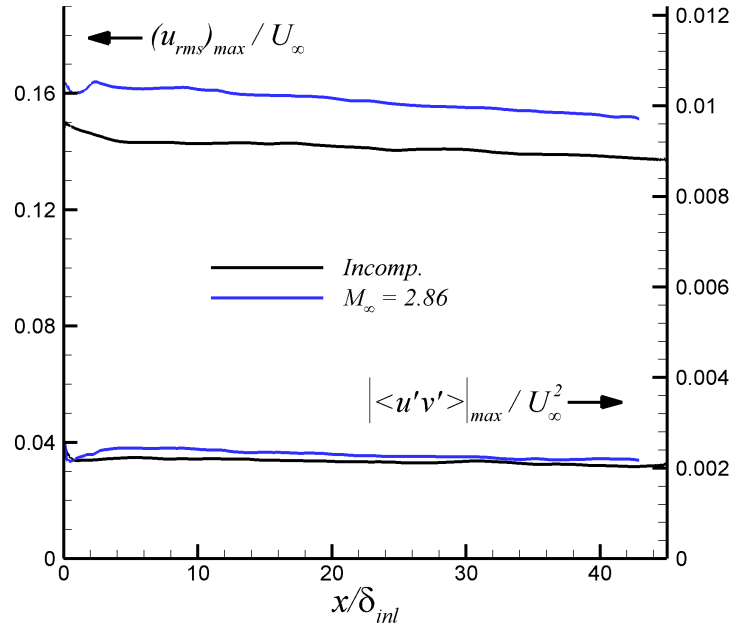

Fig. 5 Streamwise development of local maxima of streamwise velocity fluctuations and Reynolds shear stresses in the incompressible and supersonic flow cases.

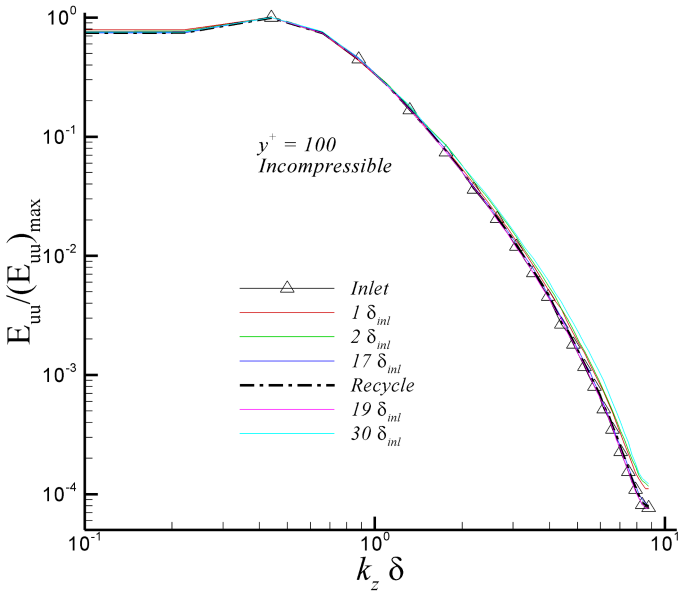

Fig. 6 Normalized spanwise energy spectra of streamwise velocity fluctuations at $y^+ = 100$ and several streamwise locations in incompressible flow.

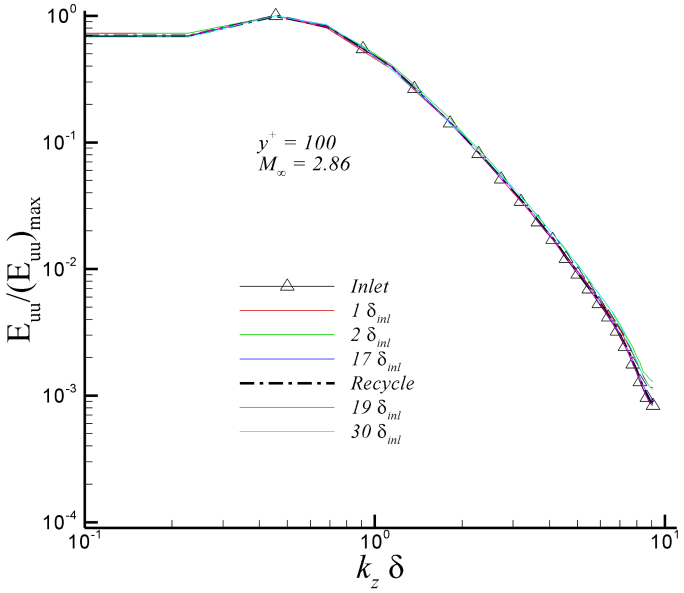

Fig. 7 Normalized spanwise energy spectra of streamwise velocity fluctuations at $y^+ = 100$ and several streamwise locations in supersonic flow.

IV. Spatial Data

A. Two-Point Correlations of Flow Fluctuations

Two-point correlations (TPC) in fluid dynamics are essential for identifying regions of spatial coherency and, indirectly, periodic regions within a flow field. These correlations offer a fundamental understanding of the interconnectedness of fluid motion over a spatial domain. In this context, we focus on the mathematical and computational methods to calculate these correlations, particularly leveraging the capabilities of the computational fluid dynamics (CFD) tool, Aquila [23]. The mathematical foundation of TPCs lies in the spatial correlation between two points within a flow field. For a turbulent flow, these correlations help in understanding the structure and dynamics of turbulence, especially in boundary layers where coherent structures play a significant role. The TPCs are calculated by considering the fluctuating components of velocity, represented as u_i' and u_j' at two different spatial points. The formulation of the two-point correlation function is given by:

$$R_{ij}(\mathbf{x}, \mathbf{r}) = \overline{u_i'(\mathbf{x} + \mathbf{r}) u_j'(\mathbf{x})} \tag{3}$$

Here, $R_{ij}(\mathbf{x}, \mathbf{r})$ represents the correlation between the velocity components i and j at two points separated by a displacement vector $\mathbf{r}$, where $\mathbf{x}$ is a reference point in space. The overbar indicates an ensemble average, which is a crucial aspect in turbulent flow analysis. To compute these correlations efficiently, especially in large and complex flow fields, a transformation to the Fourier space is employed. This approach significantly reduces computational complexity by leveraging the properties of the Fourier transform. The transformation of the fluctuating velocity component to the Fourier space is given by:

$$\mathcal{U}_i'(\mathbf{k}) = \mathcal{F}\{u_i'(\mathbf{x})\} \tag{4}$$

In this equation, $\mathcal{U}_i'(\mathbf{k})$ represents the Fourier transform of the fluctuating velocity component u_i' at a w ave vector $\mathbf{k}$. The transformation to the Fourier space allows for a more straightforward computation of the TPC by exploiting the convolution theorem. The final form of the TPC in the Fourier space can be expressed as:

$$R_{ii}(\mathbf{x}, \mathbf{r}) = \mathcal{F}^{-1}\{\mathcal{U}_i'(\mathbf{k} + \mathbf{r}) \mathcal{U}_i'^{*}(\mathbf{k})\} \tag{5}$$

Where $R_{ii}(\mathbf{x}, \mathbf{r})$ is the inverse Fourier transform of the product of $\mathcal{U}_i'(\mathbf{k} + \mathbf{r})$ and its complex conjugate $\mathcal{U}_i'^{*}(\mathbf{k})$. This formulation simplifies the calculation of TPCs by transforming the spatial correlation problem into a multiplication in the Fourier space, followed by an inverse transformation to retrieve the spatial correlation. The application of this approach, as implemented in Aquila, demonstrates efficient computation of TPCs in turbulent flows. This efficiency is crucial for studying spatially-developing turbulent boundary layers (SDTBLs) where high-resolution data is necessary. The computational efficiency of Aquila, documented in [23], not only reduces the computational load but also enhances the scalability of TPC calculations across large, complex flow domains. The practical implementation of these equations in a CFD framework involves several steps. First, the fluctuating velocity components are extracted from the flow field data. These components are then transformed into the Fourier space using a Fast Fourier Transform (FFT) algorithm. The multiplication of the transformed velocity components and their complex conjugates, followed by an inverse FFT, yields the TPCs. In the broader context of fluid mechanics, these TPCs play a pivotal role in understanding the dynamics of coherent structures within boundary layers. They provide a quantifiable measure of the spatial correlation of turbulent fluctuations, which is essential for analyzing the underlying physics of fluid flows, especially in applications involving high-speed flight and crossflow jet problems. This comprehensive approach to calculating TPCs offers a robust framework for fluid mechanics research. It not only facilitates a deeper understanding of turbulent flow structures but also contributes significantly to the development of more efficient computational methods in the field of CFD. To highlight the potential to identify spatial periodicity by using the TPC as a metric, we include a volumetric visualization of the TPC at three wall-normal distances (i.e., in the viscous linear sublayer, buffer layer and log region) in Figures 8 and 9c for the incompressible and supersonic regimes, respectively.

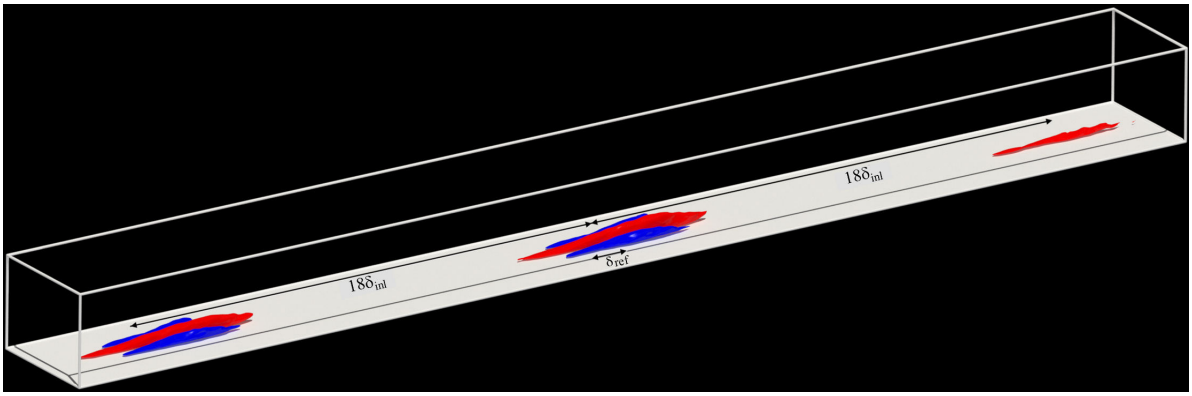

(a) $R_{u'u'}$ **at** $y^+ = 5$

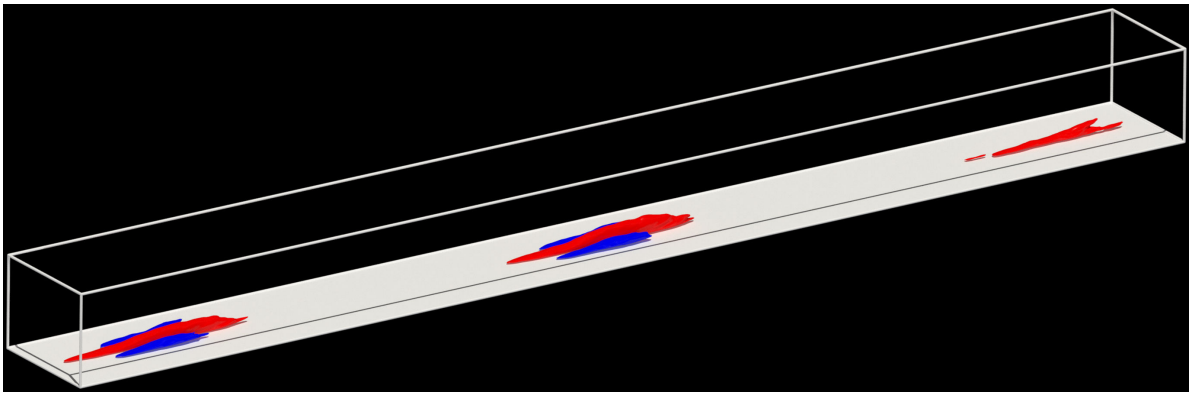

(b) $R_{u'u'}$ **at** $y^+ = 15$

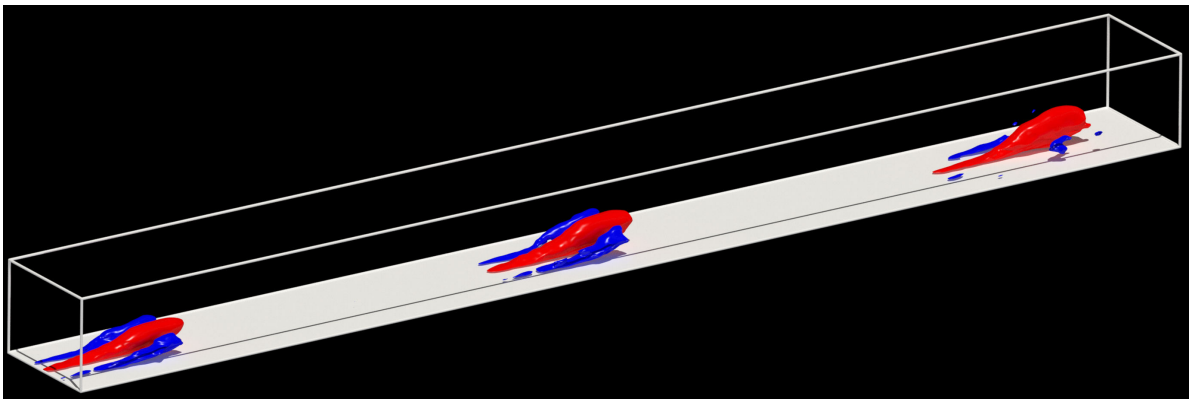

(c) $R_{u'u'}$ **at** $y^+ = 96$

Fig. 8 Two-Point Correlations for the streamwise velocity fluctuation at varying y^+ values in the incompressible flow case. Note that the structures are measured in terms of the boundary layer thickness at the point of reference (domain center) for the TPC.

The main structure (positively correlated, in red) is flanked by two sub-structures (negatively correlated, in blue) in Figures 8a-c. In all cases, the streamwise center of the domain is selected as the reference point (i.e. ref) at the different y^+ stations. It can be inferred the presence of very long and elongated (oblong-shaped main structures) turbulent structures in the near wall region ($\sim 5\delta_{ref}$). Those principal structures grow vertically as one moves further from the wall. A similar conclusion can be stated on negatively correlated sub-structures. The periodic structures both upstream and downstream from the main structure are equidistant at approximately $18\delta_{inl}$, which is the streamwise distance between the inlet and recycle plane. The consistency in the separation between the structures holds regardless of the reference point for the main structure which reinforces the theory of a period between structures. Furthermore,

the coherency between the first (upstream) structure and the main one is markedly higher than that observed with the downstream structure. Coherency in fluid dynamics refers to the degree of correlation or similarity between different regions of the flow. The reduced coherency with the downstream structure could be attributed to several factors. A primary consideration is its distance from the recycle plane, a region where the flow is reintroduced into the computational domain. The proximity to the recycle plane might influence the development and interaction of turbulent structures, leading to differences in coherency. It is also notable that the flanking structures, though negatively correlated with the main structure, exhibit a strong coherency with the upstream periodic structure. This observation suggests a complex interplay between different regions of the flow, where even inversely correlated structures can maintain a high level of coherency. Interestingly, the downstream flanking sub-structures tend to more quickly dissociate from the reference point. This phenomenon might be indicative of underlying fluid mechanisms such as vortex shedding, turbulent mixing, or wave propagation within the boundary layer.

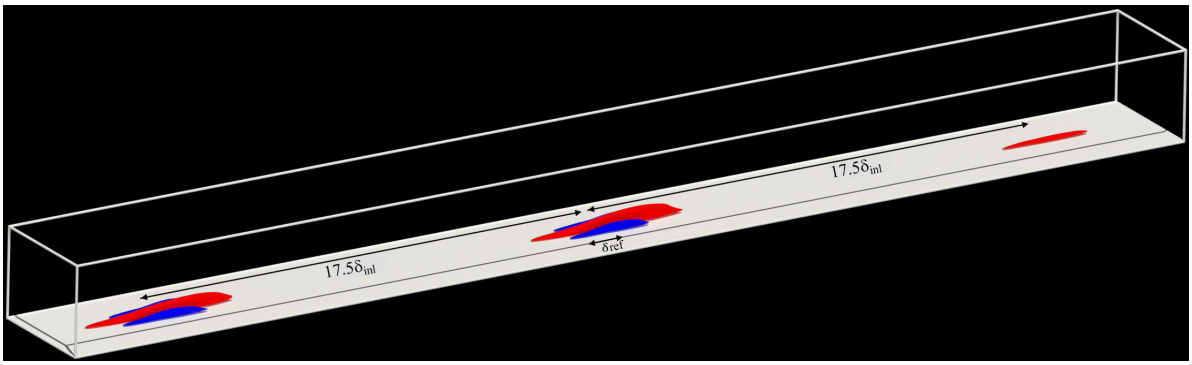

(a) $R_{u'u'}$ **at** $y^+ = 5$

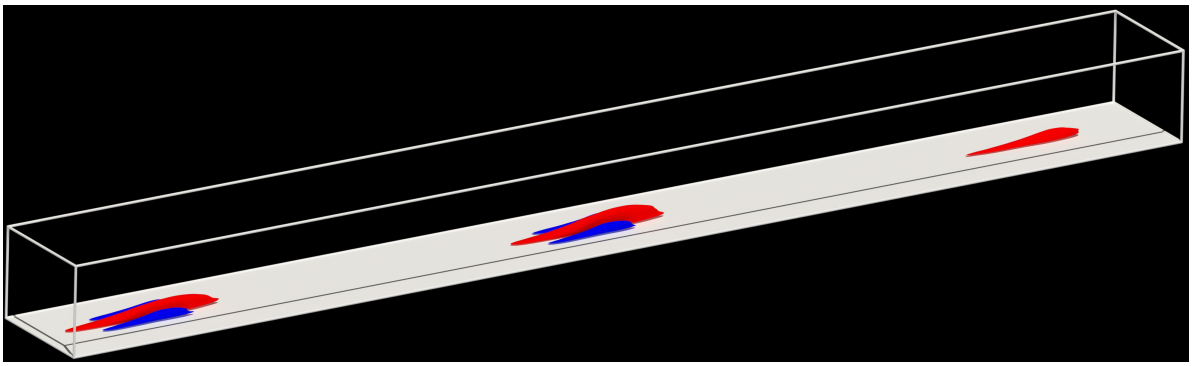

(b) $R_{u'u'}$ **at** $y^+ = 15$

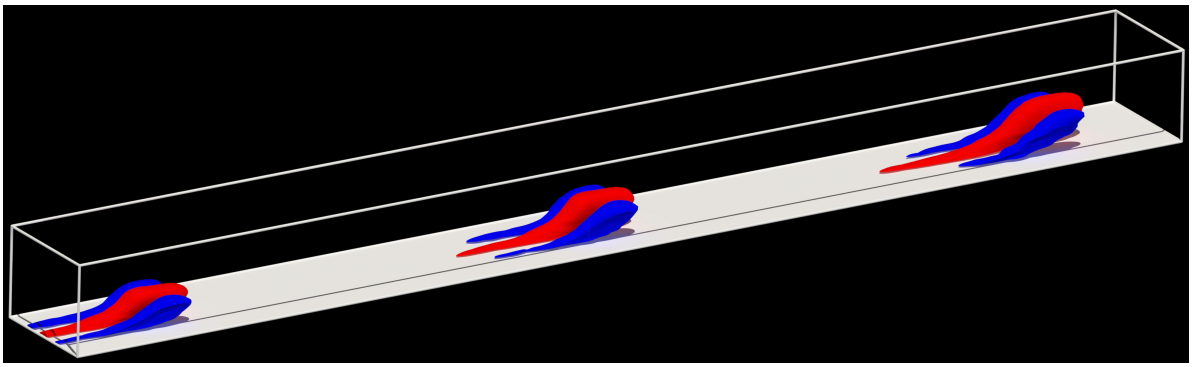

(c) $R_{u'u'}$ **at** $y^+ = 96$

Fig. 9 Two-Point Correlations for the streamwise velocity fluctuation at varying y^+ values in the supersonic flow case. Note that the structures are measured in terms of the boundary layer thickness at the point of reference (domain center) for the TPC.

In Figures 9a-c, the primary structure observed is the central structure. Similar to the incompressible case, periodic structures in the supersonic regime are present both upstream and downstream of this central feature, maintaining a consistent separation distance of approximately $17.5\delta_{inl}$ (inlet-recycle distance). Notice that streamwise lengths of turbulent structures are slightly shorter in the supersonic regime than those of the incompressible case, which can be linked to some compressibility effect. This periodicity reinforces the regular pattern within the supersonic boundary layer. The coherency between the upstream structure and the central one remains strong, indicating a robust interaction. In the absence of shock waves, the increased coherency can be attributed to the stable propagation of turbulence and flow structures within the boundary layer. The consistent separation and the high degree of correlation suggest that the flow structures are influenced primarily by the inherent dynamics of the boundary layer, such as the formation of coherent vortical structures and turbulence regeneration. The reduced coherency with the downstream structure could be influenced by the recycling boundary condition at the computational domain. This condition, where the flow is reintroduced, can lead to variations in flow characteristics that reduce the coherency downstream. Furthermore, as the structures propagate downstream, they may experience more significant dissipation and interaction with the boundary layer, leading to a decrease in their correlation with the central structure. Despite the reduced coherency downstream, the flanking structures still exhibit a strong coherency with the upstream periodic structure. This indicates a persistent and organized interaction within the supersonic boundary layer, where even negatively correlated structures maintain a significant degree of correlation with upstream features. This phenomenon suggests that the supersonic boundary layer, in the absence of shock waves, is characterized by a stable propagation of turbulence structures, coherent vortical motions, and a predictable periodicity. Overall, the supersonic flow case without shock waves demonstrates a periodic structure in the boundary layer, where the interactions between different regions of the flow are dictated by turbulence dynamics and boundary layer mechanisms rather than shock-induced effects.

B. Lagrangian Coherent Structure (LCS) Analysis

Lagrangian Coherent Structures (LCS) in fluid dynamics are pivotal for understanding the intricate behaviors within fluid flows. These structures, formed by particle trajectories, act as dynamic manifolds delineating regions of order within otherwise chaotic flow fields. Analyzing LCS provides key insights into fluid dynamics, especially in the context of mixing, transport, and diffusion processes. The methodologies for identifying and characterizing LCS are varied, with the finite-time Lyapunov exponent (FTLE) and finite-size Lyapunov exponent (FSLE) being two primary approaches. Both methods assess particle field deformation but differ in their specific focus. FSLE quantifies the time taken for a pair of particles to diverge to a set finite distance, whereas FTLE integrates deformation over a fixed, finite time regardless of particle distance. An evaluation by [24] highlighted the advantages of FTLE over FSLE. However, a comparative study by [25] demonstrated that with correct calibration, both FTLE and FSLE can yield similar results. In our work, we have leveraged the advancements made by Lagares and Araya [26]. Central to this methodology is the concept of the flow map, which traces the trajectory of a particle released at a specific time t_0 and location $\mathbf{x}_0$ within the velocity field over a certain period. The FTLE is defined as:

$$FTLE_N(\mathbf{x}, t) = \frac{1}{|N \cdot \Delta t|} \log\left(\sqrt{\lambda_{max}\left(C^t_{t_0}(\mathbf{x})\right)}\right) \tag{6}$$

Here, λ_{max} denotes the maximum eigenvalue of the right Cauchy-Green (CG) strain tensor at a given spatial coordinate $\mathbf{x}$. This tensor, essential in describing material deformation, is expressed as:

$$C_{i,j} = \frac{\partial x^t_k}{\partial x^{t_0}_i} \frac{\partial x^t_k}{\partial x^{t_0}_j}, \tag{7}$$

These derivatives measure the deformation of a particle's position relative to its initial position at t_0. The right CG strain tensor is a gauge of how a body is distorted or strained, quantifying the changes in length of material lines or fibers due to deformation. Its eigenvalues and eigenvectors represent the squared stretches and the directions of these stretches, respectively. Regions with high FTLE values indicate potential attracting or repelling manifolds. Forward time integration of particle trajectories suggests repelling manifolds, while backward integration points to attracting barriers. This distinction is crucial for dissecting the dynamics of fluid flows, particularly in turbulent environments. To delve deeper into these principles and their practical applications in fluid mechanics, further reading, such as the works of [27], is recommended. These sources offer an extensive theoretical and practical framework for understanding and applying LCS concepts in various fluid dynamics scenarios.

The results of our FTLE analysis for both incompressible and supersonic low Reynolds number cases are depicted in Figures 10 and 11. Figure 10 presents the FTLE fields for the incompressible low Reynolds number case, illustrating the attracting and repelling LCS sampled every ten flow fields. The attracting lines (Fig. 10a) and repelling lines (Fig. 10b) highlight the regions of high and low FTLE values, respectively. These structures serve as dynamic barriers to transport and mixing within the flow, with the attracting lines delineating regions where particles converge and the repelling lines identifying areas where particles diverge. The periodicity and coherence of these structures reflect the stable nature of the incompressible flow regime and the organized interaction of coherent vortices. Similarly, Figure 11 shows the FTLE fields for the supersonic low Reynolds number case. The attracting lines (Fig. 11a) and repelling lines (Fig. 11b) provide a comparative view of the LCS in a supersonic flow environment, again sampled every ten flow fields. Despite the supersonic conditions, the absence of shock waves allows for a direct comparison with the incompressible case. The FTLE patterns reveal a complex interplay of turbulence and coherent structures, with notable similarities in the periodicity and spatial distribution of attracting and repelling lines. This suggests that even at supersonic speeds, the underlying fluid mechanisms governing the formation of LCS remain consistent, with high FTLE regions marking significant barriers to mixing and low FTLE regions indicating zones of enhanced dispersion. In the supersonic low Reynolds number case depicted in Figure 11, the presence of inclined mesh lines, which are more pronounced compared to the incompressible case, can be hypothesized to result from the influence of acoustic waves. These waves, prevalent in supersonic flows, propagate through the fluid, introducing oscillations and perturbations that interact with the boundary layer. This interaction can lead to the generation of patterns that appear as inclined mesh lines in the FTLE fields. The acoustic waves may affect the coherence of the turbulent structures by inducing periodic compressions and expansions within the flow, thereby influencing the alignment and orientation of the Lagrangian Coherent Structures. This hypothesis aligns with the observed periodicity and the inclination of the mesh lines, suggesting a coupling between the flow's turbulent dynamics and the underlying acoustic wave phenomena, which does not rely on shock wave interactions but rather on the inherent compressible nature of the supersonic regime. The comparative analysis of the FTLE fields across different flow regimes underscores the utility of LCS in capturing the essential dynamics of fluid flows. The periodic structures identified in both cases are indicative of the coherent turbulent motions that govern mixing and transport processes. These findings enhance our understanding of LCS behavior in varying flow conditions and provide a foundation for future investigations into more complex flow phenomena.

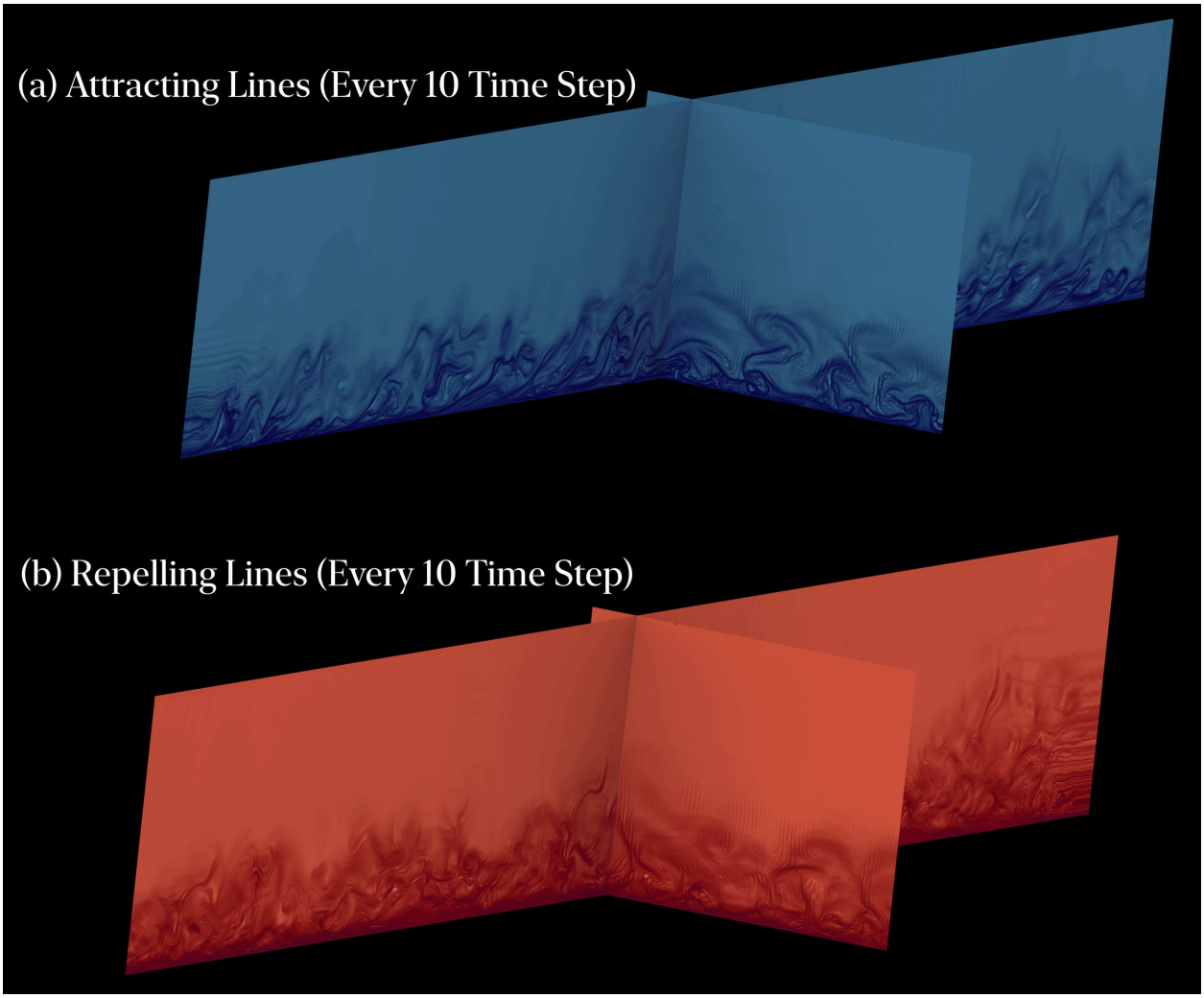

Fig. 10 Attracting and repelling FTLE based on the Incompressible Low Re case sampled every ten flow fields

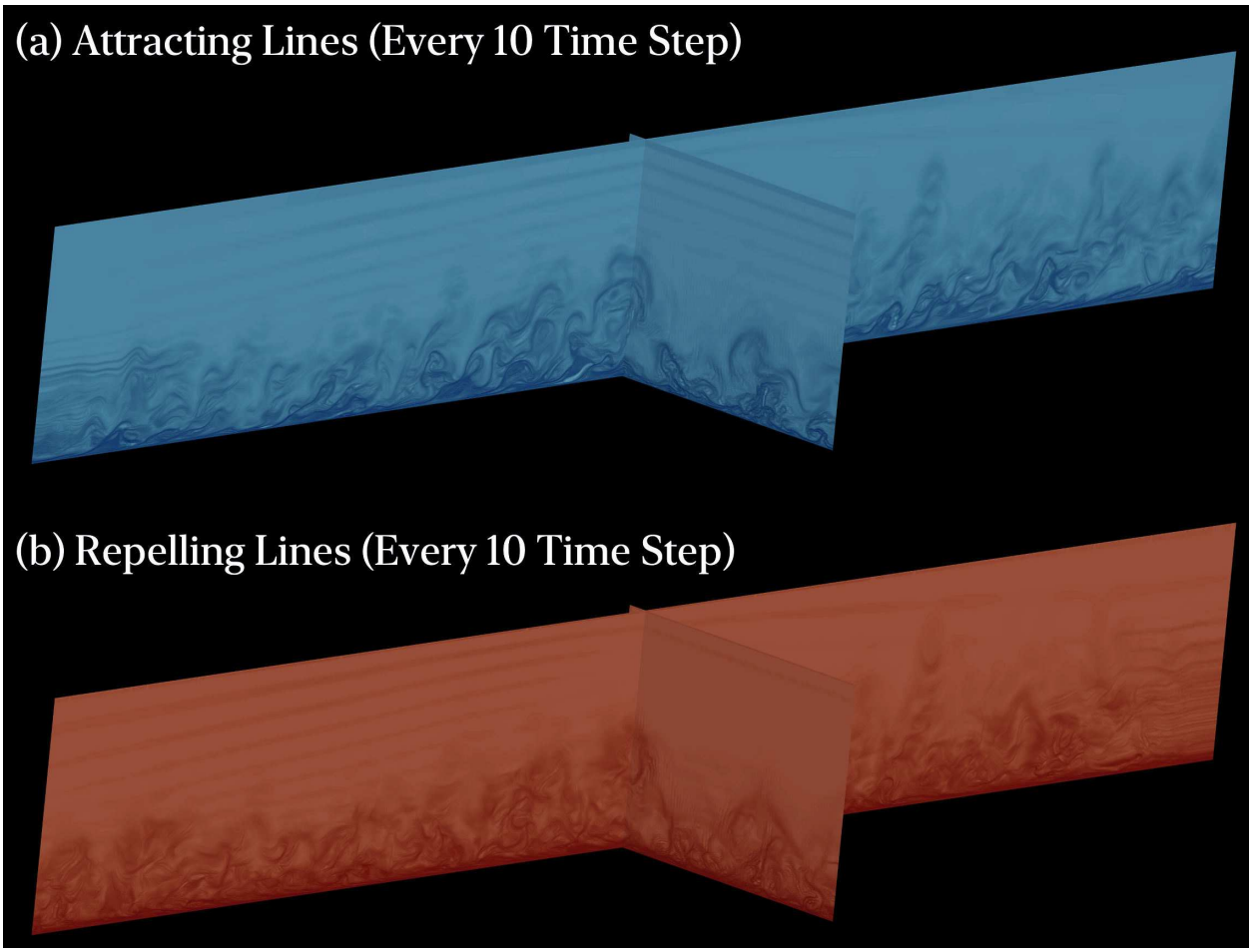

Fig. 11 Attracting and repelling FTLE based on the Supersonic Low Re case sampled every ten flow fields

V. Temporal Data

A. Time-Based Artifact Detection Methodology Description

To understand periodic events as they occur in time, the data can be transformed via a Fourier series, which takes fluctuating data as a function of time delay, τ, or frequency, f, described in (8) and (9), respectively. This transforms the data into periodic fluctuations where artifacts are found.

$$\hat{q}(\tau) = \mathscr{F}(q(t)) \tag{8}$$

$$\hat{q}(f) = \mathscr{F}(q(t)) \tag{9}$$

The magnitude of the fluctuations is best understood through the energy spectra of the various sample points in space, described in (10). This is also referred to as the energy spectral density or frequency spectra, and describes the magnitude of the fluctuations relative to their scale in time [28].

$$E = |\hat{q}(\tau)|^2 \tag{10}$$

The energy spectra will cascade from the larger motions into smaller motions as those motions break down in time [28]. This reflects the multifractal behavior mentioned previously. This cascade should conform to a certain trend, and various peaks and troughs that may deviate in small frequency ranges represent artifacts, given a lack of randomness [28]. Given that this data comes from a sample plane, and not a volume, there will be random and insignificant deviations of

various superimposed fluctuations traveling through the plane. These smaller and random deviations are smoothed by implementing a moving average filter that creates a "central limit" of these fluctuations. The random deviations in the cascade are filtered out, but the artifacts remain, as seen in Figure 12, which has a moving average filter size of 80 frequency indices. After some experimentation with the moving average filter length, 80, which also corresponds to the number of spanwise samples, appeared to remove almost all of the high frequency behavior while leaving the most prominent artifacts. Increasing this value above 80 also led to the algorithm having trouble compensating for the peak location shift due to the moving average filter.

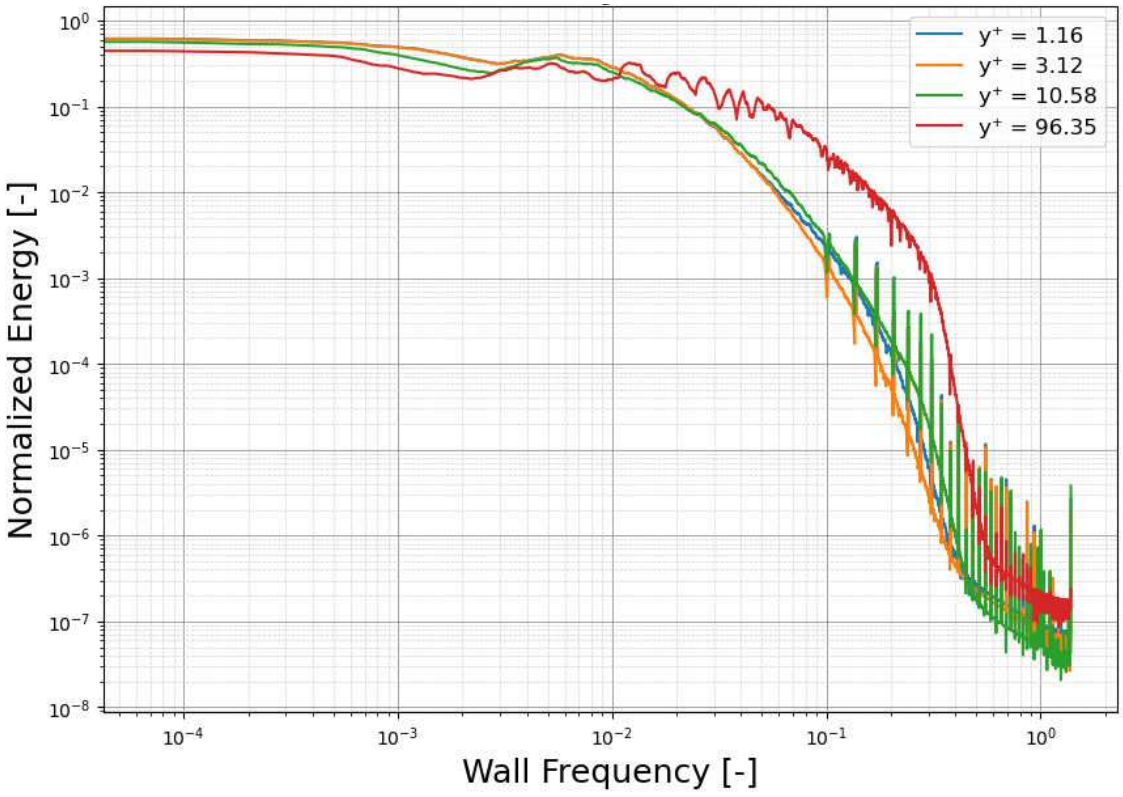

Fig. 12 Temporal energy spectra with spanwise and moving averaging Fourier space filter at recycle plane.

The SciPy toolbox [29] easily identifies these peaks. The way to find them is to set a threshold for a calculation that normalizes the area underneath the peak by the frequency where the peak is occurring at. The most prominent peaks have the largest values, and a threshold is set to filter out the minor peaks.

$$Normalized\ Area = \frac{Peak\ Height * Peak\ Width}{Peak\ Frequency} \tag{11}$$

To prove this detection method for artifacts, the peaks are filtered and re-scaled to fit into the overall trend of the energy spectra. These peaks are an assumed PDF-like distribution around their center, which the filter inverts to re-scale these peaks back into the energy spectra trend. The inverse is performed to handle troughs.

At this point in the discussion, it is helpful to transition the discussion of the energy spectra from absolute units and scale that are imposed on the DNS conditions to a set of units and scale that is common for all boundary layers. The log law of the wall provides a scaling of velocity in wall units, u^+, spatial coordinate, x^+, and time, t^+, that provide a similar scale across all boundary layers with some acceptable range [28]. This goes a step further when working with the spectral data from DNS, since the spectral data is in the form of a delay for time, or a wavenumber for space. The inner time scale is equal to ν/u_τ^2. The same applies to wavenumber, k^+. This change in scale allows users to compare

the energy spectra of different boundary layers without concern for differing conditions that may cause differences in scale close to the wall.

B. Artifacts in Energy Spectra Data

Normally the energy spectra will form the cascades shown in Figs 13 and 14. Note that in these cascades, the data is smoothed plotted in dots to lessen the effects of some of the artifacts to better show the general trend of the energy spectra, although artifacts are still present. It is also helpful to note that normalized energy refers to the energy spectral density normalized by the energy contained in the longest motion or lowest frequency, just to avoid trying to fit various scales in a small space on the page.

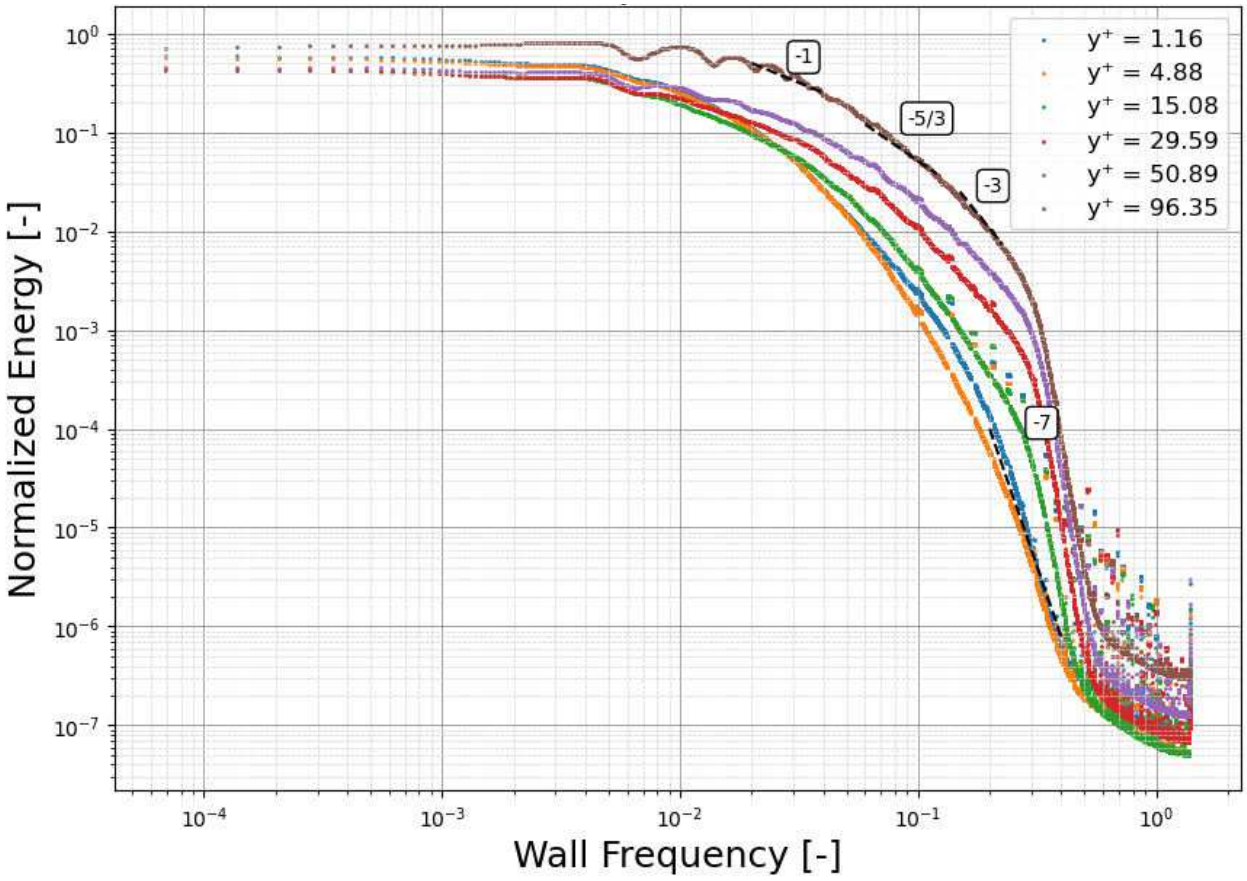

Fig. 13 Smoothed and Discrete Point u' Energy Spectra for the Incompressible Case at the Inlet Plane. Discrete points used to visually filter out spike artifacts for easier trend comparison.

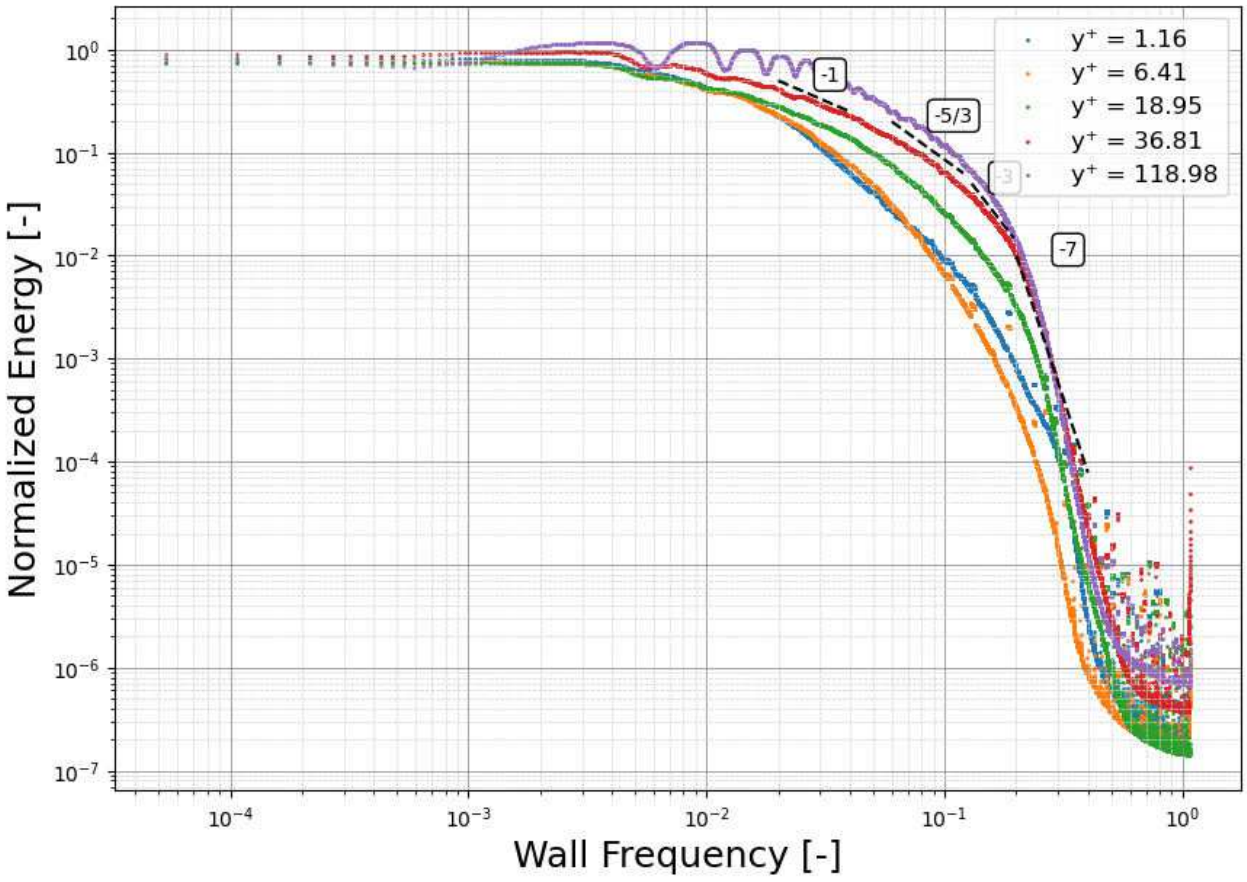

Fig. 14 Smoothed and Discrete Point u' Energy Spectra for the Supersonic Case at the Inlet Plane. Discrete points used to visually filter out spike artifacts for easier trend comparison.

When these deviations and artifacts are left in, as in Figs. 15 and 16, there are three main behaviors that are clearly present. The first are the fluctuations, or ups and downs with minor deviations from the trend. This is likely because there are fluctuations passing through the plane that are localized. Given significantly more planes or spatial span, these would likely collapse into the expected trend. The second are the spikes that appear in the dissipating and dissipated regions. These are likely artifacts of aliasing, as the Discrete Fourier Transform algorithm is picking up the same aliased samples and giving multiple response for that error in signal [30]. The span of these spike is very short, only one frequency location for the more prominent ones and two frequency locations for the more subdued spikes.

The third and most interesting trend are the humps that appear in the energy spectra. Given their fairly regular intervals, it is not entirely clear if these are related to the aliasing errors, because [31] points out that aliasing can be separate from other artifacts. Given the magnitude difference and the shape difference, it is likely a safe conclusion that these "humps" are from their own errors. These humps are also a distinctly different shape between the inner and outer boundary layer. From the autocorrelation distributions, these two areas have different behaviors in periodic behavior, and the DMA treats these regions differently and blends them [7]. The center of these peaks in the outer layer line up with the location of the recycle plane, which gives a strong indication that these effects are correlated with the recycling, and appear to dissipate with the dissipation of the turbulence when breaking down into higher frequencies. The comparison of the energy spectra between the incompressible and supersonic cases demonstrates that there is minimal difference between the two, as the artifacts are nearly in the same place in frequency due to the law of the wall scaling.

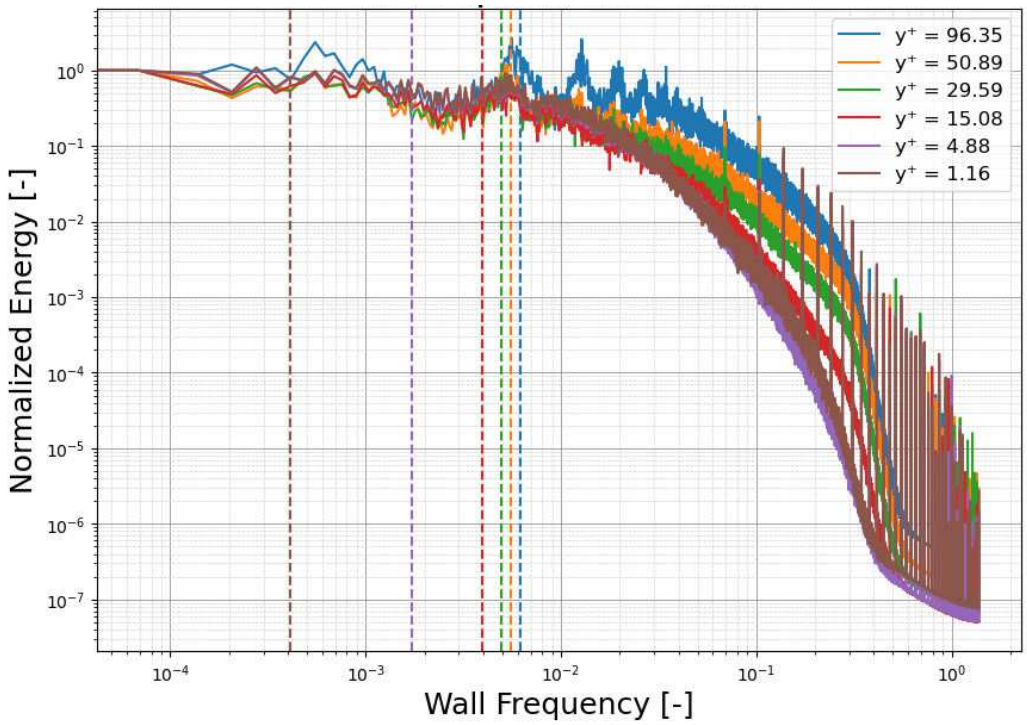

Fig. 15 u' Energy Spectra for the Incompressible Case at the Inlet Plane. Dashed vertical lines depict the distance of the recycle plane.

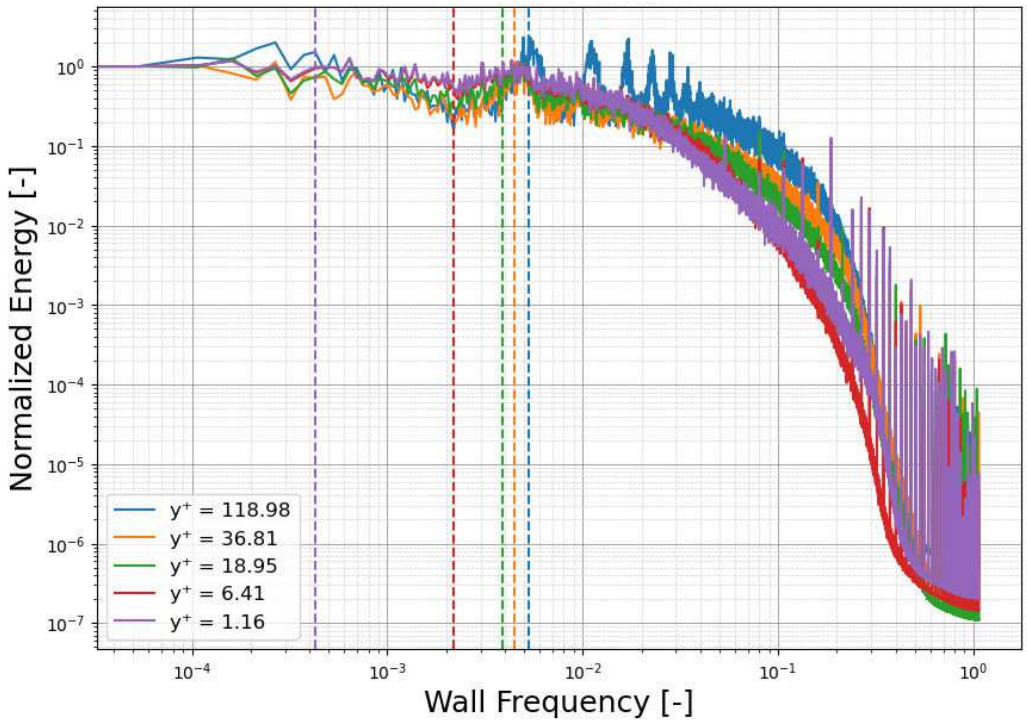

Fig. 16 u' Energy Spectra for the Supersonic Case at the Inlet Plane. Dashed vertical lines depict the distance of the recycle plane.

Figs. 17 and 18 show the energy spectra for the other velocity components, and Fig. 19 shows the energy spectra for temperature fluctuations. Most notably in all these energy contents are the same peak that correlates to the recycle length. This artifact appears and then dissipates into the cascade of turblence breakdown as with streamwise velocity fluctuations. Although, with spanwise velocity fluctuations, there appears to be a longer hump forming as the fluctuations just begin to breakdown. This may be due to some size constraints in the computational domain, or this may be another unknown effect. Alternatively, as the height in the boundary layer increases, the temperature fluctuations begin to have a sharper or flatter cascade. It is already known that the Reynolds analogy breaks down higher in the boundary layer [28], and this may be an effect of it.

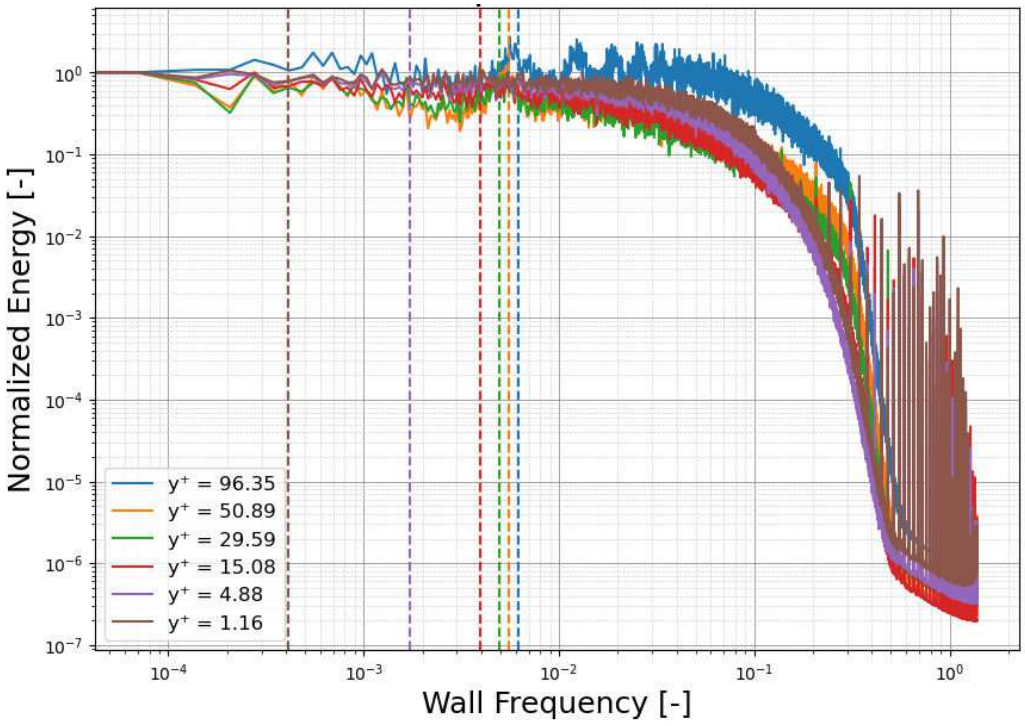

Fig. 17 v' Energy Spectra for the Incompressible Case at the Inlet Plane. Dashed vertical lines depict the distance of the recycle plane.

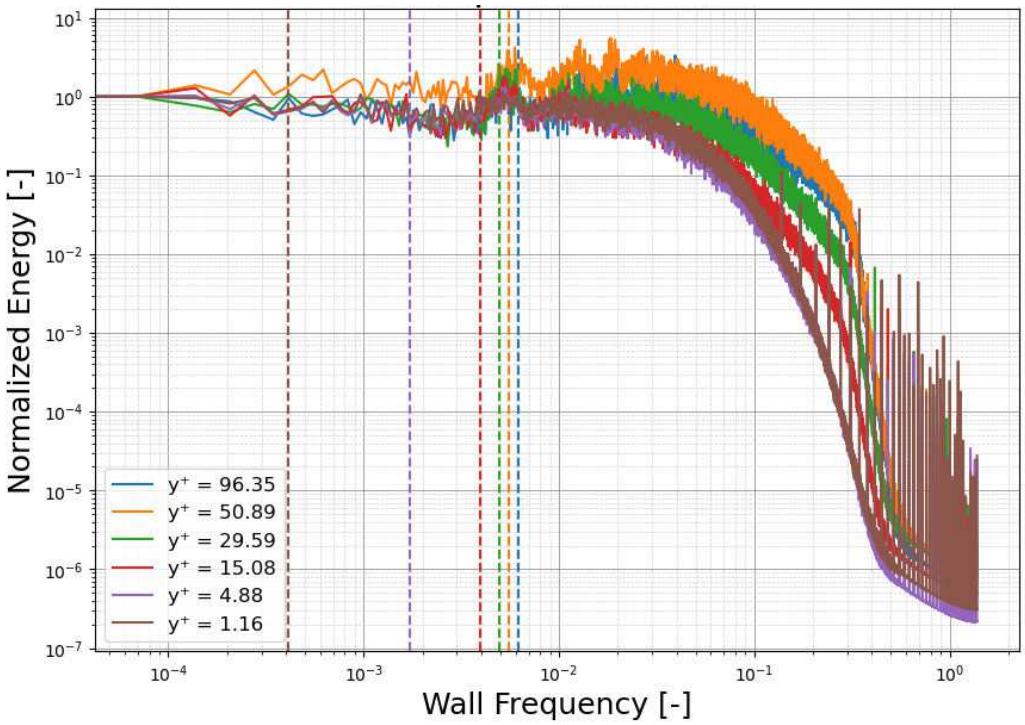

Fig. 18 w' Energy Spectra for the Incompressible Case at the Inlet Plane. Dashed vertical lines depict the distance of the recycle plane.

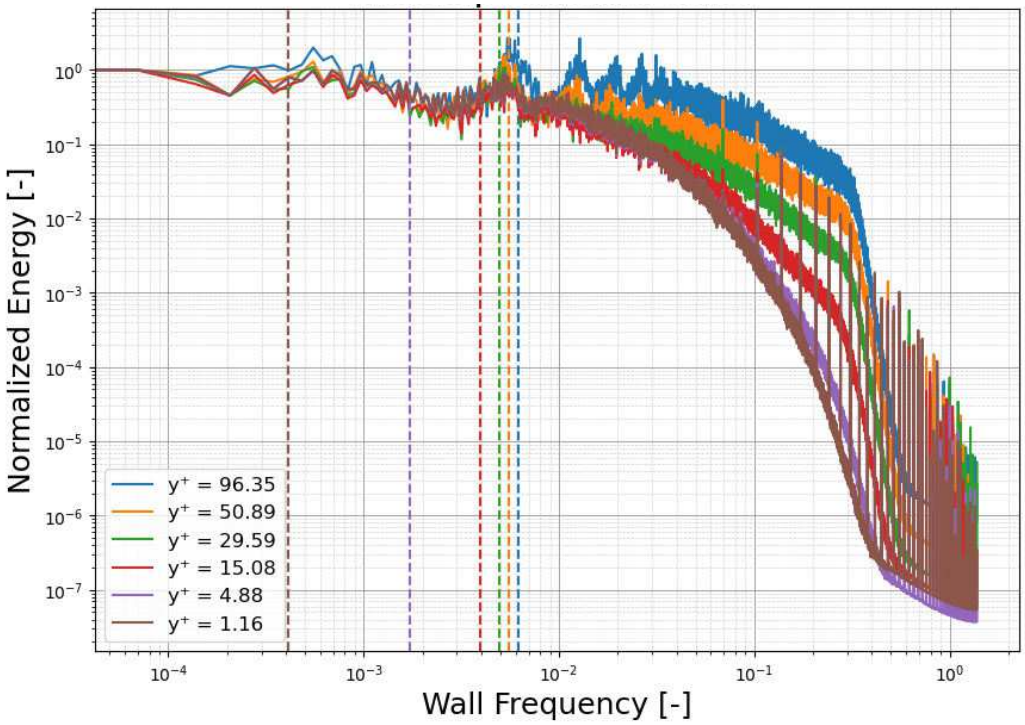

Fig. 19 t' Energy Spectra for the Incompressible Case at the Inlet Plane. Dashed vertical lines depict the distance of the recycle plane.

C. Initial Filter Design

All this data leads to the inevitable question of how one treats the data in the injected plane if there are artifacts. As an initial iteration on a filter, the following process occurs on the plane data to create a plane with minimal artifacts left by the previous flow fields.

First, the peaks and troughs are flattened, illustrated by the peaks filtered out in Fig. 20 for the energy spectra, and in Fig. 21 for a smoother energy spectra with a moving average of 80 samples applied to the same spectra. Clearly the artifacts have been removed from the spectra distribution. There are still troughs, and other more localized effects, but the bulk of the artifacts have been mitigated by this flattening.

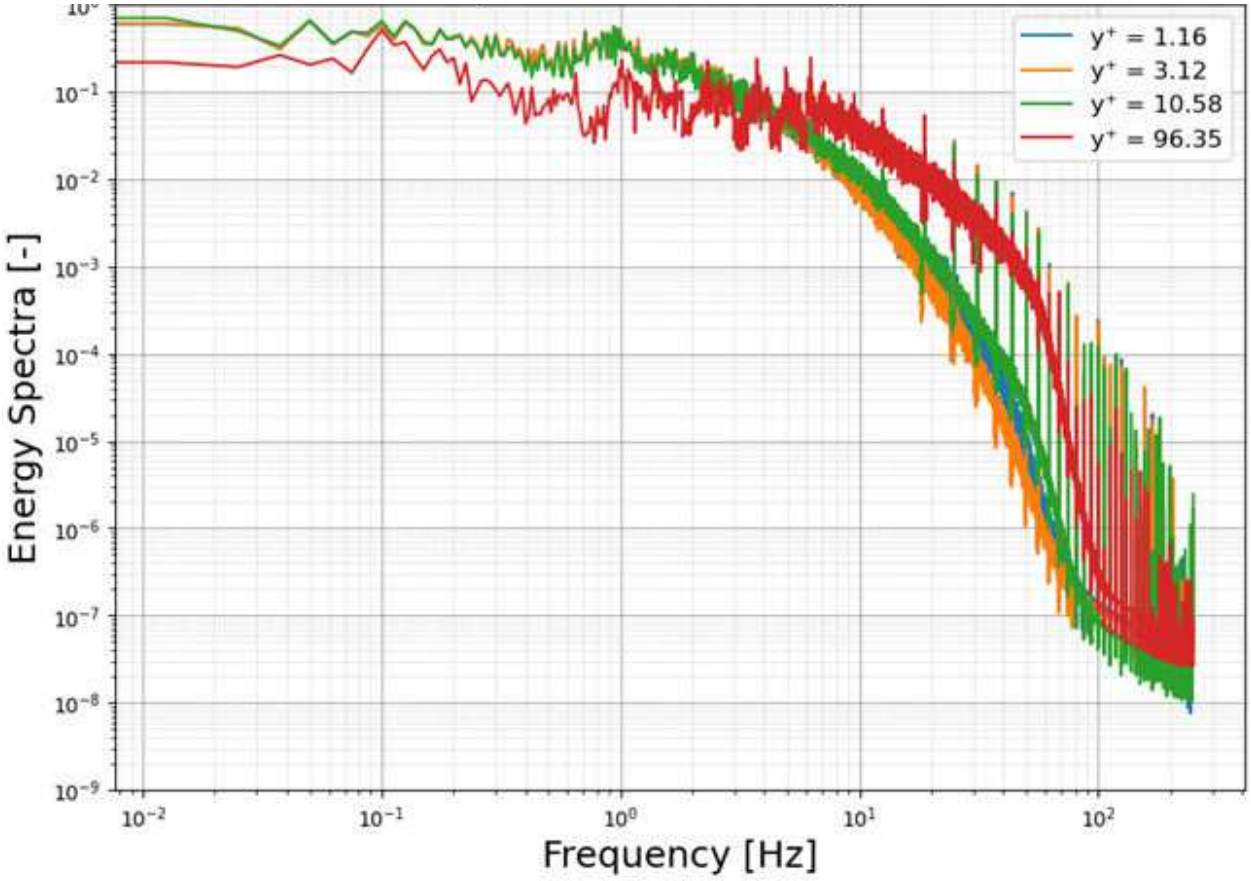

Fig. 20 u' Energy Spectra for the Incompressible Case at the Recycle Plane with Peaks Flattened.

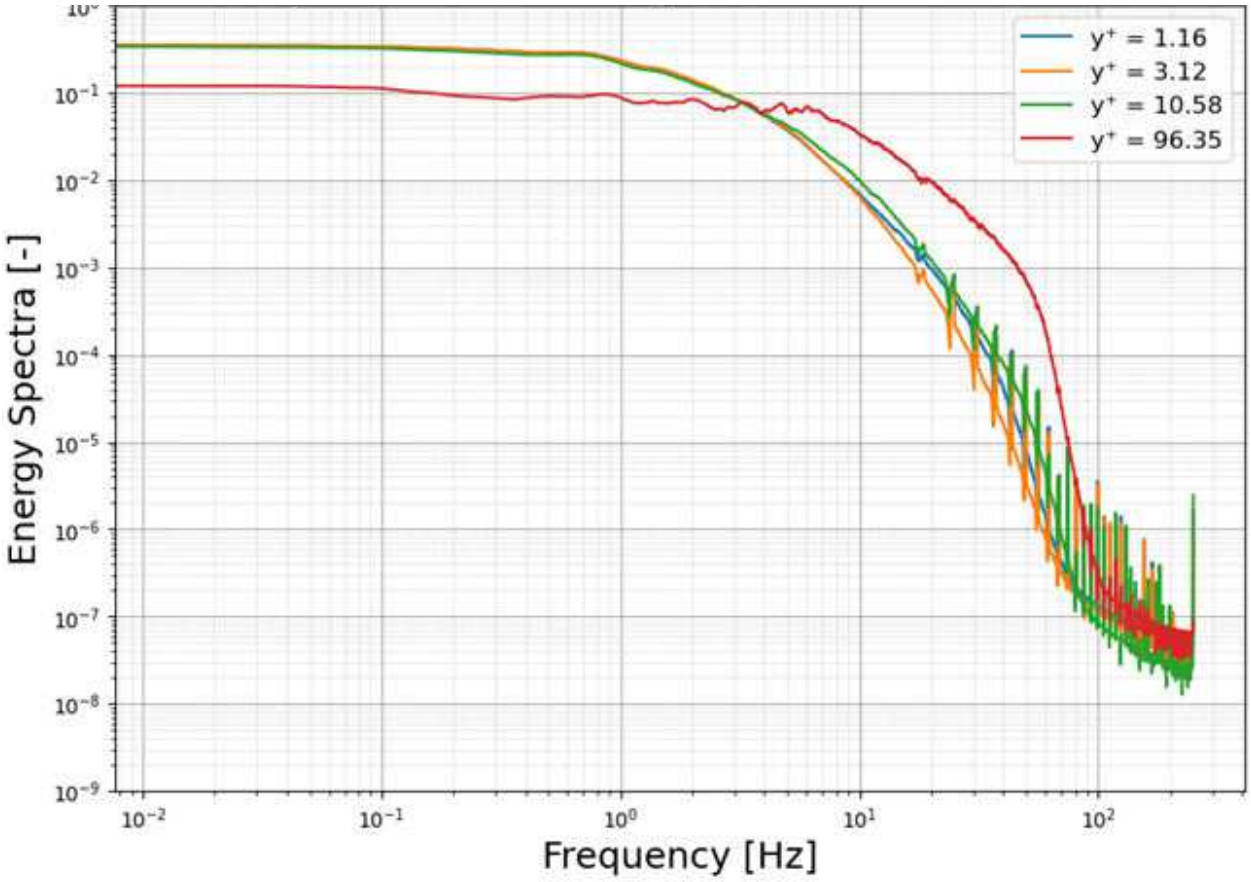

Fig. 21 u' Smoothed Energy Spectra for the Incompressible Case at the Recycle Plane with Peaks Flattened.

Second, the phase angles are fitted to a trend, which is not shown. This nearly random phase angle shift will take care of aliasing errors, but also make sure that what should be out of phase is out of phase, providing clean data for a new flow field.

Third, some other filter can be applied. In this case, an equivalent Infinite Impulse Response (IIR) filter equivalent of a moving average filter of length 2 time samples filters the spectra to mitigate the dissipated ranges of the fluctuations.

These three steps result in the autocorrelation distribution shown in Fig. 22. The peaks in the outer portion of the boundary layer are greatly diminished, meaning that the bulk of the periodic behavior observed in previous data is gone. There are still some errors present, but minor deviations will likely work themselves out as the errors themselves have been shown to dissipate. This produces data in the Fourier space that can be used to easily time step to the next flow field in the CFD solver. There are other filtering methods that can be utilized, this is just a first attempt that is more intuitive to implement.

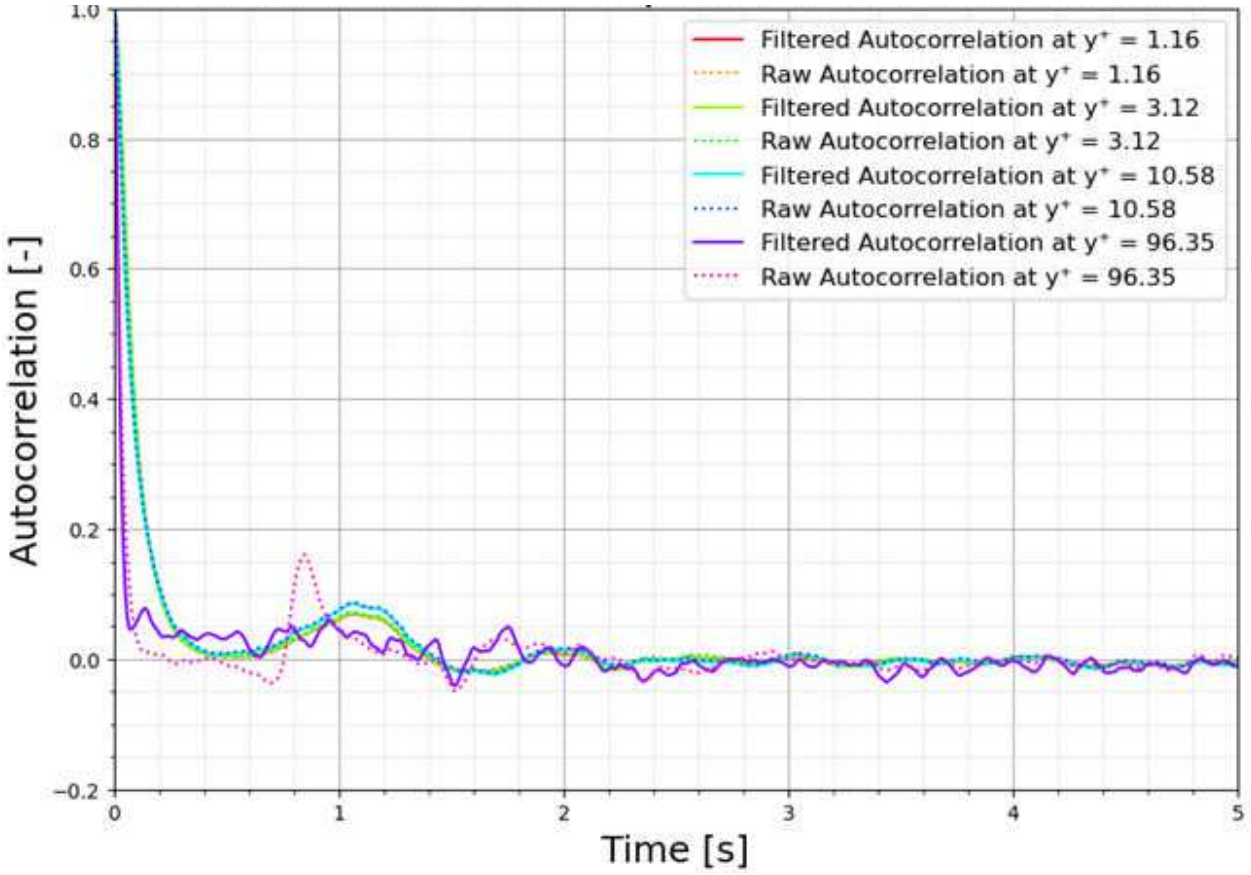

Fig. 22 u' Autocorrelation From a Filtered Plane for the Incompressible Case.

VI. Conclusion

This study undertakes a comprehensive evaluation of periodic turbulent events in spatially-developing turbulent boundary layers (SDTBL) using Direct Numerical Simulation (DNS) databases. The simulations encompass both incompressible and supersonic flow regimes under isothermal and adiabatic wall thermal conditions at low Reynolds numbers ($\delta^+ \approx 250$). Temperature is regarded as a passive scalar in the incompressible case. A type of rescaling-recycling technique for turbulent inflow generation is employed [5, 7, 32]. Our objective was to scrutinize the influence of artificially injected periodicity inherent to the recycling method on low and high-order flow statistics and the dynamics of coherent structures in zero pressure gradient (ZPG) boundary layers.

The analysis reveals several key findings. First, the application of two-point correlations demonstrates, as expected, the presence of a pronounced spatial periodicity between the inlet and recycle planes. This periodicity manifests consistently in both incompressible and supersonic cases, with periodic structures maintaining a separation distance approximately equal to the streamwise domain length between these planes. This regular separation corroborates the existence of an artificial periodicity induced by the recycling methodology, which persists primarily within the principal coherent structures, while anti-correlated flanking structures diminish more rapidly downstream. On the other hand, material attracting/repelling lines (FTLE contours) have not exhibited periodic spatial patterns due to, perhaps, the inherent particle advection scheme of the LCS methodology.

Overall, the DNS results obtained using the proposed dynamic multi-scale approach (DMA) have demonstrated an excellent agreement with external DNS data and experiments from the literature, affirming the method's validity in capturing the essential dynamics of SDTBL. Injected turbulent profiles have shown a quick adjustment (short initial developing section) to realistic boundary layer parameters, including power spectra. The Van Driest transformation effectively

accounted for compressibility effects in the supersonic case, facilitating a fair comparison with the incompressible data. These findings provide a robust foundation for future investigations into the periodic behaviors in SDTBL and the development of improved methodologies for accurate and efficient DNS of turbulent boundary layers. The turbulent energy spectra injected, extracted form the downstream flow solution and which induces a negligible developing section, makes this approach highly attractive to numerically simulate large scale systems at even higher Reynolds numbers in DNS.

Mitigation strategies for the artificial periodicity introduced by the recycling method were explored, including the use of initial filtering and Fourier-based techniques. The study's results underscore the importance of refining inflow generation methods to minimize the introduction of artificial periodic frequencies and enhance the accuracy of DNS in modeling SDTBL. Future work should focus on further discrimination between artificial and natural periodic frequencies as the next step to keep improving our turbulence precursor methodology.

Acknowledgments

This material is based upon work supported by the National Science Foundation under Grant Nos. 2314303, 1847241, HRD-1906130, and DGE-2240397, and by the Air Force Office of Scientific Research under award number FA9550-23-1-0241. This work was also supported in part by a grant from the DoD High-Performance Computing Modernization Program (HPCMP). Any opinions, findings, and conclusions or recommendations expressed in this material are those of the author(s) and do not necessarily reflect the views of the National Science Foundation, the Air Force Office of Scientific Research, or the DoD High-Performance Computing Modernization Program.

References

[1] Araya, G., Leonardi, S., and Castillo, L., "Steady and time-periodic blowing/suction perturbations in a turbulent channel flow," *Physica D: Nonlinear Phenomena*, Vol. 240, No. 1, 2011, pp. 59–77. https://doi.org/https://doi.org/10.1016/j.physd.2010.08.006, URL https://www.sciencedirect.com/science/article/pii/S0167278910002459.

[2] Saltar, G., and Araya, G., "Reynolds shear stress modeling in turbulent boundary layers subject to very strong favorable pressure gradient," *Computers Fluids*, Vol. 202, 2020, p. 104494. https://doi.org/10.1016/j.compfluid.2020.104494.

[3] Araya, G., Lagares, C., and Jansen, K., "Reynolds number dependency in supersonic spatially-developing turbulent boundary layers," *2020 AIAA SciTech Forum (AIAA 3247313) 6 - 10 January, Orlando, FL.*, 2020. https://doi.org/10.2514/6.2020-0574.

[4] Araya, G., Lagares, C., Santiago, J., and Jansen, K., "Wall temperature effect on hypersonic turbulent boundary layers via DNS," *AIAA Scitech 2021 Forum (AIAA-2021-1745)*, 2021. https://doi.org/10.2514/6.2021-1745.

[5] Lagares-Nieves, C., and Araya, G., "Power Spectrum Analysis in Supersonic/Hypersonic Turbulent Boundary Layers," *AIAA Scitech Forum*, AIAA, San Diego, CA Virtual, 2022. https://doi.org/10.2514/6.2022-0479.

[6] Liu, Q., Zhenging, L., Wang, L., Tu, G., Deng, X., and Zhou, Y., "Direct Numerical Simulations of Supersonic Turbulent Boundary Layer with Streamwise-Striped Wall Blowing," *Aerospace Science and Technology*, Vol. 441, No. 10, 2021. https://doi.org/10.1016/j.ast.2021.106510, URL https://doi.org/10.1016/j.ast.2021.106510.

[7] Araya, G., Castillo, L., Meneveau, C., and Jansen, K., "A Dynamic Multi-Scale Approach for Turbulent Inflow Boundary Conditions in Spatially Developing Flows," *Journal of Fluid Mechanics*, Vol. 670, 2011, pp. 581–605. https://doi.org/10.1017/S0022112010005616.

[8] Guarini, S., Moser, R., Shariff, K., and Wray, A., "Direct Numerical Simulation of a Supersonic Turbulent Boundary Layer at Mach 2.5," *Journal of Fluid Mechanics*, Vol. 414, 2000, pp. 1–33. https://doi.org/10.1017/S0022112000008466, URL https://doi.org/10.1017/S0022112000008466.

[9] Poggie, J., Bisek, N. J., and Gosse, R., "Resolution effects in compressible, turbulent boundary layer simulations," *Computers Fluids*, Vol. 120, 2015, pp. 57–69. https://doi.org/https://doi.org/10.1016/j.compfluid.2015.07.015, URL https://www.sciencedirect.com/science/article/pii/S0045793015002492.

[10] Wu, X., "Inflow Turbulence Generation Methods," *Annual Review of Fluid Mechanics*, Vol. 49, 2017, pp. 23–49. https://doi.org/10.1146/annurev-fluid-010816-060322, URL https://www.annualreviews.org/doi/10.1146/annurev-fluid-010816-060322.

[11] Spalart, P., "Direct Simulation of a Turbulent Boundary Layer up to R=1410," *NASA TM-89407*, Vol. N87-18030, National Aeronautics and Space Administration: Ames Research Center, Moffett Field, CA, 1986.

[12] Wu, X., Squires, K., and Lund, T., "Large Eddy Simulation of a Spatially-Developing Boundary Layer," *ACM/IEEE Conference on Supercomputing*, Association for Computing Machinery, San Diego, CA, 1995. https://doi.org/10.1145/224170.224408.

[13] Lund, T., "Generation of Turbulent Inflow Data for Spatialy-Developing Boundary Layer Simulations," *Journal of Computational Physics*, Vol. 140, 1998, pp. 233–258. https://doi.org/10.1006/jcph.1998.5882.

[14] Simens, J. J. H. S., M., and Mizuno, Y., "A High-Resolution Code for Turbulent Boundary Layers," *Journal of Computational Physics*, Vol. 228, 2009, pp. 4218–4231. https://doi.org/10.1016/j.jcp.2009.02.031, URL https://dl.acm.org/doi/10.1016/j.jcp.2009.02.031.

[15] Lee, J. H., and Sung, H. J., "Direct Numerical Simulation of a Turbulent Boundary Layer up to Re = 2500," *International Journal of Heat and Fluid Flow*, Vol. 32, 2011, pp. 1–10. https://doi.org/10.1016/j.ijheatfluidflow.2010.11.001, URL https://doi.org/10.1016/j.ijheatfluidflow.2010.11.001.

[16] Kraichnan, R., "Diffusion by a Random Velocity Field," *Physics of Fluids*, Vol. 13, 1970, pp. 22–31. https://doi.org/10.1063/1.1692799, URL https://doi.org/10.1063/1.1692799.

[17] Karweit, B.-B. P., M., and Comte-Bellot, G., "Simulation of the Propagation of an Acoustic Wave Through a Turbulent Velocity Field: A Study of Phase Variance," *Journal of the Acoustical Societ of America*, Vol. 89, 1991, pp. 52–62. https://doi.org/10.1121/1.400415, URL https://doi.org/10.1121/1.400415.

[18] Perry, A. E., and Chong, M. S., "On The Mechanism of Wall Turbulence," *Journal of Fluid Mechanics*, Vol. 119, 1982, pp. 173–217. https://doi.org/10.1017/S0022112082001311, URL https://doi.org/10.1017/S0022112082001311.

[19] Druault, L.-S. B. J.-P. C. F. D. J. L. E. L. J. F., P., and Perret, L., "Generation of Three-Dimensional Turublent Inlet Conditions for Large-Eddy Simulation," *AIAA Journal*, Vol. 42, 2004, pp. 447–456. https://doi.org/10.2514/1.3946, URL https://doi.org/10.2514/1.3946.

[20] Yousif, Z.-M. Y. L.-V. R., M., and Lim, H., "A Transformer-Based Synthetic-Inflow Generator for Spatially Developing Turbulent Boundary Layers," *Journal of Fluid Mechanics*, Vol. 957, 2023, p. A6. https://doi.org/10.1017/jfm.2022.1088, URL https://doi.org/10.1017/jfm.2022.1088.

[21] Hutchins, N., and Marusic, I., "Evidence of very long meandering features in the logarithmic region of turbulent boundary layers," *Journal of Fluid Mechanics*, Vol. 579, 2007, pp. 1–28.

[22] A.J. Smits, P. J., N. Matheson, "Low-Reynolds-number turbulent boundary layers in zero and favorable pressure gradients," *J. Ship Res.*, Vol. 27, 1983, p. 147.

[23] Lagares, C., Rivera, W., and Araya, G., "Scalable Post-Processing of Large-Scale Numerical Simulations of Turbulent Fluid Flows," *Symmetry*, Vol. 14, No. 4, 2022. https://doi.org/10.3390/sym14040823, URL https://www.mdpi.com/2073-8994/14/4/823.

[24] Karrasch, D., and Haller, G., "Do Finite-Size Lyapunov Exponents detect coherent structures?" *Chaos*, Vol. 23, No. 043126, 2013, pp. 1–11.

[25] Peikert, R., Pobitzer, A., Sadlo, F., and Schindler, B., "A comparison of Finite-Time and Finite-Size Lyapunov Exponents," *Topological Methods in Data Analysis and Visualization III*, Springer International Publishing Switzerland, 2014.

[26] Lagares, C., and Araya, G., "A GPU-Accelerated Particle Advection Methodology for 3D Lagrangian Coherent Structures in High-Speed Turbulent Boundary Layers," *Energies*, Vol. 16, No. 12, 2023. https://doi.org/10.3390/en16124800, URL https://www.mdpi.com/1996-1073/16/12/4800.

[27] Haller, G., "Distinguished material surfaces and coherent structures in three-dimensional fluid flows," *Physica D: Nonlinear Phenomena*, Vol. 149, No. 4, 2001, pp. 248–277. https://doi.org/https://doi.org/10.1016/S0167-2789(00)00199-8.

[28] Pope, S. B., *Turbulent Flows*, Cambridge Press, 2008.

[29] SciPy API Reference, *scipy.signal*, ????

[30] Blaisdell, S. E. T., G. A., and Qin, J. H., "The Effect of the Formulation of Nonlinear Terms on Aliasing Errors in Spectral Methods," *Applied Numerical Mathematics*, Vol. 21, 1996, pp. 207–219.

[31] Canuto, H. M. Y. Q.-A., C., and Zang, T. A., *Spectral Methods: Fundamentals in Single Domains*, Springer, 2006.

[32] Lagares-Nieves, C., and Araya, G., "Compressibility Effects on High-Reynolds Coherent Structures via Two-Point Correlations," *AIAA Aviation Forum*, AIAA, 2021. https://doi.org/10.2514/6.2021-2869.